14

Effect of Brittle Off-Fault Damage on Earthquake Rupture Dynamics

Marion Y. Thomas[1,2], Harsha S. Bhat[1,3], and Yann Klinger[1]

ABSTRACT

In the shallow brittle crust, following earthquake ruptures, geophysical observations show a dramatic drop of seismic wave speeds in the shallow off-fault medium. Seismic ruptures generate, or reactivate, damage around faults that alter the constitutive response of the surrounding medium, which in turn modifies the earthquake itself, the seismic radiation, and the near-fault ground motion. This numerical study aims to assess the interplay between earthquake ruptures and dynamically evolving off-fault medium and to underline the damage-related features pertinent to interpret geophysical observations. We present a micromechanics-based constitutive model that account for dynamic evolution of elastic moduli at high-strain rates. We consider 2D inplane models, with a 1D right lateral fault featuring slip-weakening friction law. We demonstrate that the response of the damaged elastic solid is different in the compressional and tensional quadrant. We observe that dynamic damage induces a reduction in elastic moduli and produces slip rate oscillations that result in high-frequency content in the radiated ground motion, consistent with strong motion records. We underline the importance of incorporating off-fault medium history in earthquake rupture processes. We find that dynamic damage generation is sensitive to material contrast and that it introduces an additional asymmetry beyond that of a bimaterial fault, in agreement with experimental studies.

14.1. INTRODUCTION

Deformation of natural fault zones in the brittle crust (~0 to 40 km depth) is conventionally perceived of as two planes, sliding one against the other, loaded by constant slip at greater depth, and whose behavior is controlled by the frictional properties of the interface [*Scholz*, 1998]. Depending on these properties, when the frictional

[1]*Institut de Physique du Globe de Paris, Université Sorbonne Paris Cité, Université Paris Diderot, Paris, France*

[2]*Department of Earth Sciences, University of Oxford, Oxford, UK*

[3]*Laboratoire de Géologie, Ecole Normale supérieure, CNRS-UMR 8538, PSL Research University, Paris, France*

resistance is overcome, the accumulated stress is released by stable sliding or by unstable dynamic events. As a consequence, in recent years, numerous studies have been carried out to determine these properties for various settings [e.g., *Byerlee*, 1978; *Scholz*, 1998; *King and Marone*, 2012; *den Hartog et al.*, 2012]. However, if the behavior of fault zones is intrinsically linked to the properties of the fault interface, it also depends on those of the surrounding medium [e.g., *Andrews*, 2005]. Fault not only consist of a fine-grained narrow fault core where slip occurs, but it is also surrounded by pervasively fractured rocks, within a complex 3D geometry.

Sibson's [1977] contribution is largely recognized as the first attempt to give a coherent description of an active fault zone. *Scholz* [2002] further proposed a slightly

different fault rock classification, which is widely used nowadays. Following the enticing review by *Biegel and Sammis* [2004], one can use the Punchbowl fault zone as a representative model of "mature" strike-slip faults that have recorded large displacement. Fault zone may be then idealized as an intricate structure consisting of a fault core, surrounded by a damage zone. Based on the revised description of the Punchbowl fault structure by *Chester et al.* [1993], the fault core comprises an inner layer of ultracataclasite bounded by an outer layer of foliated cataclasite. The extremely fine-grained core material is then surrounded by a damage zone that includes layers of gouge and breccia bordered by fractured rocks. The last two layers are included in the damage zone because they lacked extensive shearing [*Chester et al.*, 1993; *Biegel and Sammis*, 2004]. Evidently, there are significant variations from one fault zone to another, but they share in common a highly fine-grained fault core (often extremely narrow band), where most of the displacement has occurred, surrounded by a damaged wall rock. However, the gouge and breccia layer is missing along various faults [*Biegel and Sammis*, 2004].

Systematic micro- and macrostructural field studies have recently been performed on damage zones [*Shipton and Cowie*, 2001; *Faulkner et al.*, 2006; *Dor et al.*, 2006; *Mitchell and Faulkner*, 2009; *Faulkner et al.*, 2011; *Savage and Brodsky*, 2011] as a key component to understand the energy balance of earthquakes [e.g., *Rice*, 2002; *Kanamori*, 2006]. The width of the damage zone is determined by measuring the decay in crack intensity away from the fault core, until it falls to the background level of the host rock [e.g., *Chester and Logan*, 1986; *Biegel and Sammis*, 2004; *Faulkner et al.*, 2011]. The fractured rocks usually have a spatial scale of the order of meters to kilometers; however, this is difficult to define and particularly time consuming. Hence, there are few field surveys focused on the structure of the damage zone. Among them, several studies in low-porosity rocks (crystalline, sedimentary rocks) have highlighted an exponential decay of crack density away from the fault [*Vermilye and Scholz*, 1998; *Wilson et al.*, 2003; *Mitchell and Faulkner*, 2009; *Faulkner et al.*, 2006, 2011], or alternatively, that the decay could be fit using a power law [*Savage and Brodsky*, 2011]. As underlined by *Faulkner et al.* [2011], the trend is less clear for faults developed in higher porosity rocks [*Shipton and Cowie*, 2001]. Possible mechanisms responsible for the development of off-fault damage could include the fault geometry, the linking of structures, the quasi-static stress field, the process zone associated with fault growth, and the coseismic fracture damage [*Vermilye and Scholz*, 1998; *Rice et al.*, 2005; *Childs et al.*, 2009; *Faulkner et al.*, 2011; *Vallage et al.*, 2015]. In their study of the Bolfín fault in northern Chile, *Faulkner et al.* [2011]

discussed several processes that could explain the development of the observed scaling inside the fault zone and concluded that the spatial extent of damage might be better explained by the damage zone growth with increasing displacement, due to geometric irregularities, or by coseismic damage.

Fault zone structure is of key importance in the mechanics of faulting. In fact, several studies have underlined the importance of the fault zone fabric in controlling the slip behavior of fault zones [*Collettini et al.*, 2009; *Niemeijer et al.*, 2010; *Thomas et al.*, 2014a; *Audet and Burgmann*, 2014; *Klinger et al.*, 2016]. For example, *Audet and Burgmann* [2014] recently highlighted a direct relation between the properties of the overlying forearc crust in subduction zones and the average recurrence time of slow earthquakes. Along the Longitudinal Valley fault in Taiwan, a structural analysis and a kinematic study have demonstrated that the damaged forearc formation favors aseismic creep, whereas the locked segments of the fault are in contact with intact rocks, or the protolith [*Thomas et al.*, 2014b, a]. Fault zone structure is equally important during seismic slip. The complexity of the fault zone system impacts the rheological properties of the fault core and the surrounding medium, both of which influence the seismogenic behavior of the fault. The changes in elastic stiffness of the bulk control the amount of elastic strain energy that can be stored during tectonic loading and released during earthquakes and can induce a stress rotations (due to contrasting elastic moduli with the host rock), allowing faults to slip under less-optimal far-field stress conditions [*Faulkner et al.*, 2006]. During seismic faulting, the stress concentration at the tip of the rupture generates, or reactivates, damage (fractures) around faults that modifies the microstructure and the constitutive response of the surrounding medium [e.g., *Rice et al.*, 2005]. Seismic ruptures can trigger a significant coseismic drop in velocity (reduction in elastic stiffness of up to 40%), on spatial scales of hundreds of meters normal to the fault and a few kilometers along depth, followed by a time-dependent recovery over a couple of years [*Hiramatsu et al.*, 2005; *Li et al.*, 2006; *Brenguier et al.*, 2008; *Cochran et al.*, 2009; *Froment et al.*, 2014]. In turn, the coseismic change in elastic moduli influences the rupture itself, which has a direct effect on the size of the earthquake, the radiated waves field, and near-fault ground motion [*Walsh*, 1965a, b; *Faulkner et al.*, 2006; *Bhat et al.*, 2012]. Therefore, recognizing the evolution of damage during earthquakes is critical to understanding the nucleation, propagation, and arrest of earthquakes. This numerical study in particular aims to explore intricate feedbacks between the spontaneous off-fault damage generation and the dynamic rupture propagation.

Numerous studies in the last couple of decades have explored the effect of off-fault plasticity on seismic

rupture, using either analytical approaches [*Rice et al.*, 2005; *Ngo et al.*, 2012] or numerical simulations (see following references). Some models have explored the effect of damage on the properties of the dynamic rupture (mode, speed, and directivity) and final slip by prescribing a low-velocity zone around the fault [e.g., *Kaneko and Fialko*, 2011; *Cappa et al.*, 2014; *Huang et al.*, 2014]. Another set of models uses a Mohr-Coulomb [e.g., *Andrews and Harris*, 2005; *Ben-Zion and Shi*, 2005; *Hok et al.*, 2010; *Gabriel et al.*, 2013] or Drucker-Prager [e.g. *Templeton and Rice*, 2008; *Ma*, 2008; *Dunham et al.*, 2011] yield criterion to investigate dynamic rupture propagation with spontaneous dynamic formation of off-fault damage. In their studies, *Yamashita* [2000] and *Dalguer et al.* [2003] model the generation of off-fault damage as the formation of tensile cracks, using a stress- and fracture-energy-based criterion, respectively. If these types of study provide a good insight on the effect of damage structure on seismic rupture, they do not account for dynamic changes of elastic moduli in the medium and therefore do not completely model the feedbacks between the off-fault damage and the seismic rupture. Determining the constitutive behavior of the surrounding medium requires developing models based on the mechanics of cracks and how they respond to the applied loading. It requires using an energy-based approach to develop the new constitutive law [e.g., *Lyakhovsky et al.*, 1997a; *Finzi et al.*, 2009; *Suzuki*, 2012; *Xu et al.*, 2014; *Lyakhovsky and Ben-Zion*, 2014]. In particular, these models need to include a physical crack growth law to model the evolution of damage. Ideally, this law should incorporate the loading rate crack-tip velocities dependency of fracture toughness [*Chen et al.*, 2009; *Dai et al.*, 2010, 2011; *Wang et al.*, 2010, 2011; *Zhang and Zhao*, 2013], which is particularly important to model earthquake-related processes. The latter constitutes the essential difference between the model presented in this chapter and the models aforementionned.

The development of the constitutive model is presented in section 14.2, followed by a description of the numerical method and the parameters we used for this chapter. In the third section we consider three different scenarios to explore the interplay between earthquake rupture and off-fault damage, how it affects both the hosting medium and the rupture propagation, and what the damage-related features are that can be pertinent to interpret geophysical observations. Our findings are summarized in section 14.5.

14.2. CONSTITUTIVE MODEL

This numerical study aims to explore the effect of spontaneous off-fault damage generation on dynamic rupture propagation. This section provides the description of the constitutive model used to account for the dynamic

Table 14.1 Parameters of the damage constitutive model.

Parameter	Symbol	Equation
Angle to σ_1 for microcracks	Φ	eq. 12
Projection of a to σ_1	α	$\cos\Phi$
Damage variable	D	eq. 13
Initial damage variable	D_0	eq. 11
Stress intensity factor	K_I	eq. 21, 27
Dynamic stress intensity factor	K_I^d	*Bhat* [2012], eq. 43
Dynamic initiation toughness	K_{IC}^D	*Bhat* [2012], eq. 45
Dynamic fracture toughness	K_{IC}^d	*Bhat* [2012], eq. 46
Instantaneous wing-crack speed	$v \equiv \mathrm{d}l/\mathrm{d}t$	*Bhat* [2012], eq. 50
Stress	σ_{ij} or $\boldsymbol{\sigma}$	eq. 32, 35, 41
Stress invariant	σ, τ	*Bhat* [2012], eq. 11
Strain	ε_{ij} or $\boldsymbol{\varepsilon}$	eq. 6, 15
Strain invariant	ε, γ	eq. 30

evolution of elastic properties in the surrounding medium, related to dynamic off-fault damage. The different parameters and constants used for the constitutive model are summarized in Table 14.1.

14.2.1. Energy-Based Approach: General Considerations

The micromechanical method used in this study followed an energy-based approach to determine the constitutive strain-stress relationship of a damaged solid, as defined by *Rice* [1971], *Hill and Rice* [1973] and *Rice* [1975]. In other words, to account for fracture damage, we create an energetically equivalent solid. This formalism, thermodynamically argued, was developed to model the inelastic behavior at macroscopic scale that arises from specific structural rearrangements at microscale, such as twinning in crystals, grain-boundary-sliding, phase transformation, or microcrack development. This approach relates inelastic deformation of a given solid to a sequence of constrained equilibrium states, characterized by the values of strain ε, temperature T, and internal variables ξ (such as damaged state). Then the relation between these properties and macroscopic stress are determined by fixing the internal variables at their current values for each imaginary equilibrium state, for which elastic constitutive law can therefore be applied. In practice, internal variables will have a time-dependent evolution, determined by the local conditions, but the kinetic aspect of it is taken care of separately (see section 14.2.7). Hence, the formalism of equilibrium thermodynamics can be adopted and using the properties of thermodynamic potentials, local

structural rearrangement can be related to corresponding changes in the macroscopic stress and strain state [*Rice*, 1971].

Let $\boldsymbol{\varepsilon}$ denote the strain tensor for an arbitrary equilibrium state and let $\boldsymbol{\sigma}$ be the corresponding stress tensor such that $\boldsymbol{\sigma} d\boldsymbol{\varepsilon}$ is the work per unit volume for any virtual deformation $d\boldsymbol{\varepsilon}$. The variable ξ denotes the current "inelastic" state of the material. Following the thermodynamic principles, we can therefore write:

$$\sigma = \sigma(\varepsilon, T, \xi). \tag{14.1}$$

The basic assumption is that work potential

$$W^H = W^H(\varepsilon, T, \xi) \tag{14.2}$$

exists at each ξ within the associated ε domain. Then for any strain variation $\delta\boldsymbol{\varepsilon}$ at fixed ξ, i.e., for which we obtain purely elastic deformation, we can write:

$$\sigma\delta\varepsilon = \delta W^H(\varepsilon, T, \xi), \tag{14.3}$$

and therefore, we can determine the stress tensor as follows:

$$\sigma = \frac{\partial W^H(\varepsilon, T, \xi)}{\partial \varepsilon}. \tag{14.4}$$

Within the elastic domain for any given ξ, W^H actually corresponds to Helmotz free energy [*Rice*, 1971]. The complementary potential is the Gibbs free energy, so that

$$W^G = W^G(\sigma, T, \xi) = \sigma : \varepsilon - W^H \tag{14.5}$$

and

$$\varepsilon = \frac{\partial W^G(\sigma, T, \xi)}{\partial \sigma}. \tag{14.6}$$

Variations in state at fixed ξ, noted $\delta\boldsymbol{\varepsilon}$, $\delta\Psi$, etc., should be reversible (path independent). More general variations that involve a change $d\xi$ are defined by $d\boldsymbol{\varepsilon}$, $d\Psi$, etc. In particular, let $d\Psi^i$ denote the change in the free energy function when the solid undergoes deformation that takes it from state ξ to state $\xi + d\xi$ at constant σ and T:

$$dW^{G_i} = W^G(\sigma, T, \xi + d\xi) - W^G(\sigma, T, \xi) \tag{14.7}$$

Therefore, the inelastic strain associated with $d\xi$, by differentiating equation (14.7), is given by

$$d^i\varepsilon_{ij} = \frac{\partial}{\partial \sigma_{ij}}(dW^{G_i}). \tag{14.8}$$

Thus, inelastic variations in the potentials are themselves potentials for inelastic variations in stress and strain [*Rice*, 1971]. As for the full strain increment, we can write that

$$d\varepsilon_{ij} = M_{ijkl}d\sigma_{kl} + \alpha_{ij}dT + d^i\varepsilon_{ij}, \tag{14.9}$$

the first term corresponding to the purely elastic strain and the second to the thermoelastic effect, with the compliance tensor $\boldsymbol{M}$ given by

$$M_{ijkl} = \frac{\partial^2 W^G(\sigma, T, \xi)}{\partial \sigma_{ij}\partial \sigma_{kl}}. \tag{14.10}$$

Hence, following this framework, we can develop a damage-constitutive model that accounts for inelastic deformation. The following section (14.2.2) defines the internal variable (ξ) used in our micromechanical model to describe the inelastic state, and then using the energy-based approach, we develop a constitutive strain-stress relationship (section 14.2.5).

14.2.2. Inelastic Deformation in the Brittle Crust Is Largely Controlled by the Presence of Preexisting Fractures

Inelastic deformation in the brittle crust occurs by nucleation, growth, and/or sliding on preexisting "fractures" at different scales. Fractures includes faults and joints but also smaller scale cracks and flaws such as mineral twins or defects in the crystal structure, grain boundaries, and pores. Frictional sliding occurs under compressive stress on preexisting fractures when the shear stress overcomes the frictional resistance acting on the fracture interface. Tensile cracking, on the other hand, can have different origins. Under regional tensile loading, the stress concentration allows the local stresses at the crack tips to exceed the rock strength, leading to crack propagation. Tensile cracking can also occur by hydraulic cracking: locally, the pore pressure increase can lead to tensile stresses at the crack tips, even under compressive loading. Finally, frictional sliding on fractures under compression creates a tensile force (as the faces slide in opposing direction) that opens wing cracks at the tip of the shear fractures. The wing cracks nucleate and grow in σ_1 direction (most compressive) and open in σ_3 direction (least compressive).

Flaws described above (e.g., fractures, microcracks, faults, mineral defects, grain boundaries, pores), are found in all natural rocks. Therefore, for the purpose of this study, and following *Ashby and Sammis* [1990], and *Deshpande and Evans* [2008], we represent the medium surrounding faults as an isotropic elastic solid that contains preexisting monosized flaws, here represented
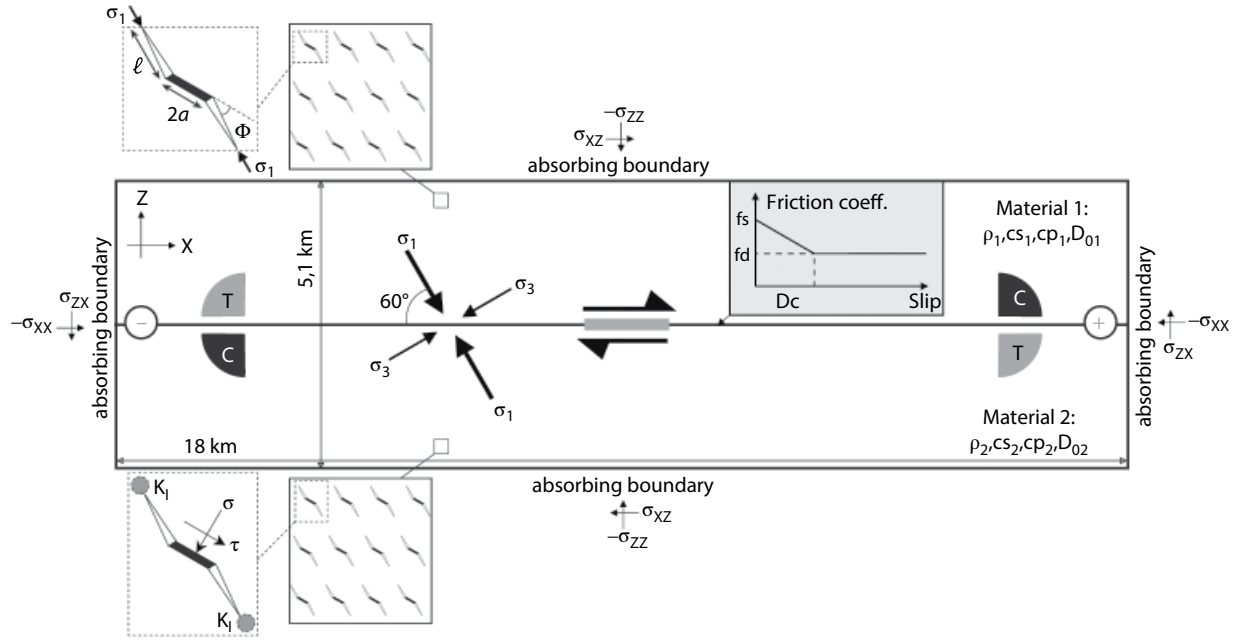
Figure 14.1 Schematics and parameters for simulations of dynamic ruptures in a 2D inplane model. We consider a right-lateral planar fault (black line in the middle), embedded in a brittle off-fault medium with a damage-constitutive law. Material properties are defined by the density (ρ), the S- and P-waves speed (c_s and c_p), and the initial damage density (D_0). In some simulations, we assume a material contrast across the fault. In that case, material 1 is always the softer material, and material 2 the stiffer. Slip-weakening friction (gray box) acts on the 18 km long fault, C and T denoting the compressional and the tensional quadrants, respectively. Also shown are the "+" and "−" directions defined by the material contrast across the fault. The "+" direction is defined as the direction of motion of the more compliant material (M2 in our case). The medium is loaded by uniform background stresses with the maximum compressive stress σ_1 making an angle of 60° with the fault plane. The thick gray line corresponds to the nucleation-prone patch where the initial shear stress is set up to be just above the fault strength.

by penny-shaped cracks of radius a (Figure 14.1). They are assumed to have a volume density N_v (prescribed) that remains fixed during the loading (i.e., no nucleation of new cracks). The density of these initial flaws per unit volume is characterized by a scalar D_0 defined as

$$D_0 = \frac{4\pi}{3} N_v (\alpha a)^3, \qquad (14.11)$$

where αa is the projection of the crack radius parallel to the direction of σ_1. We only take into account the cracks that are optimally oriented from a Coulomb friction perspective for a given stress state, i.e., the cracks are aligned at the same angle Φ to the largest (most negative) remote compressive stress, σ_1 (see *Bhat et al.* [2011] for a justification):

$$\Phi = \frac{1}{2} \tan^{-1} (1/f), \qquad (14.12)$$

where f is the coefficient of friction.

Under suitable conditions, inelastic deformation occurs in the model by either opening the preexisting cracks or by propagation of cracks. For simplicity, we account for opening and propagation of cracks due to regional tensile loading and frictional sliding (compressive loading), but we do not include hydrofracturing in the model. Cracks grow in the form of tensile wing cracks that nucleate at the tips of the penny-shaped flaws. Wings cracks, each of length l, grow parallel to the σ_1 axis (Figure 14.1), and the current damage state is then defined by the scalar D (fraction of volume occupied by micro-cracks):

$$D = \frac{4\pi}{3} N_v (\alpha a + l)^3. \qquad (14.13)$$

D approaching 1 corresponds to the coalescence stage that leads to the macroscopic fracture of the solid. Henceforth, the internal variable D, which describes the current damage state of our solid, denotes the inelastic state of the material (replacing ξ in section 14.2.1).

14.2.3. Gibbs Free Energy of a Damage Solid

In this chapter, we use the aforementioned energy-based framework (section 14.2.1) to determine the strain-stress relationship of a damaged solid by defining the constitutive relationship in terms of Gibbs free energy W^G. Henceforth, we assume isothermal conditions, and the Gibbs free energy density of a damaged solid, for a given stress state σ and damage state D, can be written as the sum of (i) the free energy $W^{G_e}(\sigma)$ of a solid, without flaws, deforming purely elastically and (ii) the free energy $W^{G_i}(\sigma, D)$ corresponding to the contribution of microcracks :

$$W^G(\sigma, D) = W^{G_e}(\sigma) + W^{G_i}(\sigma, D). \qquad (14.14)$$

Consequently, the associated elastic and inelastic strains, ε_{ij}^e and ε_{ij}^i, respectively, can be expressed as:

$$\varepsilon_{ij} = \varepsilon_{ij}^e + \varepsilon_{ij}^i = \frac{\partial W^{G_e}(\sigma)}{\partial \sigma_{ij}} + \frac{\partial W^{G_i}(\sigma, D)}{\partial \sigma_{ij}}. \quad (14.15)$$

Properties of the linear elastic material are described by its shear modulus μ, Poisson's ratio v, and mass density ρ. The elastic strain energy density is given by

$$W^{G_e}(\sigma) = \frac{1}{4\mu}\left[2\tau^2 + \frac{3(1-2v)}{(1+v)}\sigma^2\right]. \qquad (14.16)$$

Then, since all cracks in our model have the same orientation, the Gibbs function associated with inelastic deformation at constant σ can be written in terms of the Gibbs free energy per crack $\Delta W^G(\sigma, D)$ times the number of cracks per unit volume (N_v):

$$W^{G_i}(\sigma, D) = N_v \Delta W^G(\sigma, D). \qquad (14.17)$$

The Gibbs free energy per crack depends on the fracture energy release rate G (crack growth) and the surface energy γ_s (to create a surface):

$$\Delta W^{G_i}(\sigma, D) = N_v \Delta W^G(\sigma, D), \qquad (14.18)$$

where ds describes the position along the microcrack and Γ corresponds to the locus of all crack fronts. Based on fracture mechanics, for an isotropic elastic solid, the energy release rate G can be related to the stress intensity factors at the tip of the crack by

$$G(\sigma, D) = \frac{1-v^2}{E}\left[K_I^2(\sigma, D) + K_{II}^2(\sigma, D) + \frac{K_{III}^2(\sigma, D)}{(1-v)}\right], \qquad (14.19)$$

where E is the Young's modulus. However, under dynamic loading rates, the wing cracks quickly quit mode II and mode III to become purely tensile. As a consequence, their contributions are neglected in this model. We also neglect the work done by the starter flaws. The total Gibbs free energy of the damaged solid can thus be approximated as

$$W^G(\sigma, D) = W^{G_e}(\sigma) + N_v\int_\Gamma\left[\frac{1-v^2}{E}K_I^2(\sigma, D) - 2\gamma_s\right]ds. \qquad (14.20)$$

The evaluation of the Gibbs free energy, and thus the mechanical constitutive description of the modeled brittle material, is hence based on the evaluation of the stress intensity factor K_I at the tip of the microcracks inside the solid (see section 14.2.4).

14.2.4. Evaluating the Stress Intensity Factors at the Tip of the Crack

To account for the energy "lost" in the medium due to inelastic deformation in the brittle crust, we therefore need to compute the stress intensity factor K_I. Once the loading is sufficiently large to induce inelastic deformation, it does so by opening preexisting cracks or by propagation of cracks. Based on structural observations (see section 14.2.2), we defined three regimes, depending on the overall stress-state: one for tensile loading and two for compressive loading. Under Regime I (compressive loading), stresses are not high enough to allow sliding or opening of the microcracks. Hence, the solid is assumed to behave like an isotropic linear elastic solid, and therefore $W^{G_i}(\sigma, D)$ is assumed to be zero. Still for compressive loading, Regime II is reached when the shear stress τ overcomes the frictional resistance $f(-\sigma)$ acting on microcracks. Then, as previously described, inelastic deformation is accounted for by growing tensile wing cracks at the tip of the penny-shaped cracks. Finally, our model also accounts for the overall remote tensile loading (Regime III). In that particular case, both penny-shaped cracks and wing cracks open due to normal tensile stress.

Under Regime II (compressive loading), the mode I stress intensity factor K_I^{R-II} for a unit volume containing N_v cracks of size $(l + \alpha a)$ can be expressed as

$$K_I^{R-II}(\sigma, D) = \sqrt{\pi a_0}\left[A(D)\sigma + B(D)\tau\right], \quad (14.21)$$

where σ and τ correspond to the first invariant of the stress tensor and the second invariant of the deviatoric stress tensor, respectively (equation [14.11] in *Bhat et al.* [2012]). The parameters A and B both depend on the damage variable, with

$$A(D) = fc_1(D) + c_3(D)\left[fc_2(D) + 1 \right] \quad (14.22)$$

$$B(D) = c_1(D) + c_2(D)c_3(D) \quad (14.23)$$

and

$$c_1(D) = \frac{\sqrt{1-\alpha^2}}{\pi\alpha^{3/2}\left[(D/D_0)^{1/3} - 1 + \beta/\alpha \right]^{3/2}} \quad (14.24)$$

$$c_2(D) = \left(\frac{\sqrt{1-\alpha^2}}{\alpha} \right)\left(\frac{D_0^{2/3}}{1-D^{2/3}} \right) \quad (14.25)$$

$$c_3(D) = \frac{2\sqrt{\alpha}}{\pi}\left[(D/D_0)^{1/3} - 1 \right]^{1/2} \quad (14.26)$$

Regime III prevails under tensile loading, and the stress intensity factor K_I^{R-II} is a quadratic function of the stress invariants:

$$K_I^{R-III}(\sigma,D) = \sqrt{\pi a_0}\left[C^2(D)\sigma^2 + O^2(D)\tau^2 \right]^{1/2} \quad (14.27)$$

with

$$C(D) = A + \Omega\sqrt{\alpha\left[D/D_0 \right]^{1/3}} \quad (14.28)$$

$$O(D) = \sqrt{\frac{B^2 C^2}{C^2 - A^2}}. \quad (14.29)$$

14.2.5. Determining the Constitutive Stress-Strain Relationship

Following the energy-based approach described in sections 14.2.1 and 14.2.3, we can define the constitutive stress-strain relationship for a damage solid. The Gibbs free energy function $W^G(\sigma D)$ is determined by computing the stress intensity factors K_I as described in section 14.2.4, depending on the regime. Then, following equations (14.6) and (14.10), W^G is differentiated once with respect to stress to obtain the strain-stress relationship, and twice with respect to stress to get the compliance tensor. The Gibbs free energy can also be expressed in terms of the conjugate strains invariants:

$$\varepsilon = \varepsilon_{kk} \quad \text{and} \quad \gamma = \sqrt{2e_{ij}e_{ij}} \quad \text{with} \quad e_{ij} = \varepsilon_{ij} - \frac{\varepsilon}{3}\delta ij,$$
$$(14.30)$$

which gives the Helmotz free energy, W^H (see equation [14.5]). Differentiating twice $W^H(\varepsilon, D)$ with respect to strain will then give the stiffness tensor C_{ijkl}.

14.2.5.1. Constitutive Relationship for Regime I

Under Regime I, there is no sliding or opening of the microcracks. Therefore, the Gibbs free energy is given by

$$W^G(\sigma,D) = W^{G_e}(\sigma) = \frac{1}{4\mu}\left[2\tau^2 + \frac{3(1-2v)}{(1+v)}\sigma^2 \right], \quad (14.31)$$

and the strain-stress relationship follows linear elasticity:

$$\sigma_{ij} = 2\mu\left[\varepsilon_{ij} + \frac{v}{1-2v}\varepsilon\delta_{ij} \right] = 2\mu\varepsilon_{ij} + \lambda\varepsilon\delta_{ij}, \quad (14.32)$$

where λ is the Lamé's first parameter.

14.2.5.2. Constitutive Relationship for Regime II

For Regime II and III, following equation (14.20), the Gibbs free energy can be written as the sum of the elastic contribution, $W^{G_e}(\sigma)$, and the inelastic contribution due to the presence of microcracks, $W^{G_i}(\sigma,D)$ (see equation [14.20]). Following *Deshpande and Evans* [2008] and *Bhat et al.* [2012], we assume that the constants A and B of K_I^{R-II} and C and O of K_I^{R-III} are only a function of the ratio l/a (and not l and a separately), and therefore we can treat them as constants. We thus find that the Gibbs free function for Regime II can be approximated by

$$W^G(\sigma,D) = W^{G_e}(\sigma) = \frac{1}{4\mu}\left[A_1\sigma + B_1\tau \right]^2, \quad (14.33)$$

where

$$A_1 = A\sqrt{\frac{\pi D_0(1-v)}{\alpha^3}} \quad \text{and} \quad B_1 = B\sqrt{\frac{\pi D_0(1-v)}{\alpha^3}};$$
$$(14.34)$$

If we state the above expression in terms of conjugate strains (ε and γ), we obtain the Helmotz free energy that can be differentiated once with respect to strain to obtain the stress-strain relation:

$$\sigma_{ij} = \frac{\mu}{\Gamma}\left\{ \left(\frac{3(1-2v)}{(1+v)} + A_1^2 - \frac{A_1 B_1 \varepsilon}{\gamma} \right)\varepsilon_{ij} \right.$$
$$\left. + \left(\frac{3v}{(1+v)} + \frac{B_1^2}{2} - \frac{A_1^2}{3} + \frac{A_1 B_1 \varepsilon}{3\gamma} \right)\varepsilon\delta_{ij} - \left(\frac{A_1 B_1}{2} \right)\gamma\delta_{ij} \right\}$$
$$(14.35)$$

with
$$\Gamma = \left[\frac{3(1-2v)}{2(1+v)} + \frac{3(1-2v)}{4(1+v)} + \frac{A_1^2}{2} \right]. \quad (14.36)$$

Based on equation (14.35), we can define the equivalent Lamé parameters μ^* and λ^*:

$$\mu^* = \frac{\mu}{2\Gamma}\left(\frac{3(1-2v)}{(1+v)} + A_1^2\right) \quad \text{and} \quad \lambda^* = \frac{\mu}{\Gamma}\left(\frac{3v}{(1+v)} + \frac{B_1^2}{2} - \frac{A_1^2}{3}\right),$$
(14.37)

and therefore approximate the change in waves speed occurring in the medium:

$$c_p^* = \sqrt{\frac{\lambda^* + 2\mu^*}{\rho}} \quad \text{and} \quad c_s^* = \sqrt{\frac{\mu^*}{\rho}}.$$
(14.38)

14.2.5.3. Constitutive Relationship for Regime III
Under Regime III, the Gibbs free energy is given by

$$W^G(\sigma, D) = W^{G_e} + \frac{1}{4\mu}\left[C_1^2\sigma^2 + O_1^2\tau^2\right], \quad (14.39)$$

where

$$C_1 = C\sqrt{\frac{\pi D_0(1-v)}{\alpha^3}} \quad \text{and} \quad O_1 = O\sqrt{\frac{\pi D_0(1-v)}{\alpha^3}}; \quad (14.40)$$

If we state the above expression in terms of conjugate strains, and differentiating the obtained Helmotz free energy W^H with respect to strain, we can derive the the constitutive relationship

$$\sigma_{ij} = \mu\left\{\left(\frac{4}{2+O_1^2}\right)\varepsilon_{ij} + \left(\frac{2}{\frac{3(1-2v)}{(1+v)} + C_1^2} - \frac{4}{3\left[O_1^2 + 2\right]}\right)\varepsilon\delta_{ij}\right\}.$$
(14.41)

Following the same logic as for Regime II, we can define the equivalent Lamé parameters μ^* and λ^*:

$$\mu^* = \mu\left(\frac{4}{2+O_1^2}\right) \quad \text{and} \quad \lambda^* = \mu\left(\frac{2}{\frac{3(1-2v)}{(1+v)} + C_1^2} - \frac{4}{3\left[O_1^2 + 2\right]}\right),$$
(14.42)

and therefore compute the change in wave speed occurring in the medium.

14.2.6. Criteria for Regime Transition

Criteria to determine the regimes to be applied in the model are defined based on the stress intensity factor K_I. In Regime I the stresses are not sufficient to allow inelastic deformation (sliding or opening of the microcracks). This implies $K_I \leq 0$ at the tip of the cracks (K_I^{RII} or K_I^{RIII}, since C and O are related to A and B). Therefore, based on equation (14.21), the criteria for Regime I is

$$A\sigma + B\tau \leq 0. \quad (14.43)$$

For the two regimes (II and III) undergoing inelastic deformation, K_I is positive and the transition between regimes is obtained by ensuring the continuity of conjugate plastic strains ε^i and γ^i. Following equation (14.8), the conjugate plastic strains are derived as $\varepsilon^i = \partial W^{G_i}/\partial\sigma$ and $\gamma^i = \partial W^{G_i}/\partial\tau$. The first invariant of the plastic strain tensor corresponds to the opening of the microcracks, whereas the second invariant is related to the frictional sliding of the penny-shaped cracks. Under compressive loading, tensile deformation only occurs by opening of the wing cracks, whereas under Regime III, both penny-shaped cracks and wing cracks open due to normal tensile stress. As a consequence, ε^i is smaller for compressive loading (Regime II) than for tensile loading (Regime III). Therefore, we are in Regime II when

$$A\sigma + B\tau > 0 \quad \text{and} \quad \left(A^2 - C^2\right)\sigma + AB\tau > 0 \quad (14.44)$$

and Regime III is reached for

$$A\sigma + B\tau > 0 \quad \text{and} \quad \left(A^2 - C^2\right)\sigma + AB\tau < 0. \quad (14.45)$$

14.2.7. Dynamic Crack Growth Law

In the previous sections, we have developed the constitutive laws that prescribe the response of a damaged solid to a remote tensile or compressive loading. The energy-based approach used in this model requires computing of the Gibbs free energy, $W^G(\sigma, D)$, which depends on the stress tensor and the microcrack density D per unit volume (section 14.2.3). Therefore, we need to define the state of cracks in the medium, or how they respond to remote loading, since as cracks grow, the state parameter D also increases (equation [14.13]), which in turn affects the constitutive response of the material (section 14.2.5). To complete the constitutive model, we thus define a state evolution law for the parameter D. Differentiating equation (14.13) with respect to time leads to

$$\frac{dD}{dt} = \left(\frac{3D^{2/3}D_0^{1/3}}{\alpha a}\right)\frac{dl}{dt}, \quad (14.46)$$

where $dl/dt \equiv v$ corresponds to the instantaneous wing-crack tip speed. We adopt the crack growth law developed by *Bhat et al.* [2012] that accounts for loading rate dependent fracture initiation toughness, K_{IC}^D [*Wang et al.*,

2010, 2011; *Zhang and Zhao*, 2013], and propagation toughness, K_I^d [*Chen et al.*, 2009; *Dai et al.*, 2010, 2011; *Zhou and Aydin*, 2010; *Gao et al.*, 2015].

14.3. NUMERICAL METHOD AND MODEL DESCRIPTION

14.3.1. Numerical Method

This study aims to evaluate the influence of the dynamic evolution of damage in the surrounding medium on seismic ruptures. Therefore, the constitutive damage model described above has been implemented in the 2D spectral element code SEM2DPACK [*Ampuero*, 2002, available at http://web.gps.caltech.edu/~ampuero/software.html]. Reactivation of damage depends on the state of stress in the medium, which in turn is influenced by the dynamic evolution of damage density (see section 14.2.5). Hence, to realize the micromechanics-based model, in the context of dynamic rupture, we developed a constitutive update scheme that takes into account this intricate feedback, using a Runge-Kutta-Fehlberg (RKF) method to integrate equation (14.46). Between each time step during the simulations, for a given a strain field (ε), we solve for the new damage density field D using an RKF update. Then, given this new value of the state parameter, we solve for the stress field (σ) using the damage constitutive law (section 14.2.5).

14.3.2. Model Setup

In our simulations, we consider a 2D inplane model with a 1D right lateral fault embedded in a brittle off-fault medium that allows for dynamic evolution of elastic moduli (Figure 14.1). To simplify the problem, we assume plane strain conditions. In our simulations, the medium is loaded by uniform background stresses. The maximum compressive stress σ_1 and the minimum compressive stress σ_3 are in the $x - z$ plane, whereas the intermediate principal stress σ_2 coincides with σ_{yy}. The fault plane makes a 60° angle with σ_1, and we assume a uniform normal stress ($\sigma_0 = \sigma_{zz}^0$) and shear stress ($\tau_0 = \sigma_{xz}^0$) distribution on the fault, except for the nucleation-prone patch (thick gray line in Figure 14.1), for which we assign a value slightly above the nominal static strength (section 14.3.3). Finally, to warrant any interference with the propagating dynamic rupture, we set the domain (5.1×18 km) large enough and we apply absorbing boundary conditions on the edge of the computation domain. Reference values for the different parameters are summarized in Table 14.2.

14.3.3. Friction Law and Nucleation Procedure

Rupture propagation along the fault plane is governed by a slip-weakening friction law [e.g. *Palmer and Rice*, 1973]. Slip occurs when the on-fault shear stress reaches the shear strength $\tau = f(-\sigma^*)$ (see section 14.3.4 for a definition of σ^*). The friction coefficient f depends on the cumulated slip (δ) and drops from a static (f_s) to a dynamic (f_d) value over a characteristic distance δ_c:

$$f = \begin{cases} f_s - \left(f_s - f_d \right)\delta/\delta_c & \text{if} \quad \delta \leq \delta_c \\ f_d & \text{if} \quad \delta > \delta_c \end{cases}. \quad (14.47)$$

In our models, we set the static friction coefficient at 0.6, which corresponds to a value measured in laboratory

Table 14.2 Input parameters for our simulations.

Parameter	Symbol	Value	
Normal stress on the fault (MPa)	σ_0	60.7	
Shear stress on the fault (MPa)	τ_0	19.9 or 36.4	
Static friction coefficient	f_s	0.6	
Dynamic friction coefficient	f_d	0.1	
Characteristic slip (m)	δ_c	1	
Prakash and Clifton [1993] time (s)	t^*	40×10^{-3}	
Poisson's ratio	v	0.276	
Branching speed (km.s^{-1})	v_m^{ss}	1.58	
Quasi-static fracture toughness	K_{IC}^{ss}	1.2×10^6	
Ashby and Sammis [1990] factor	β	0.1	
Crack factor	Ω	2.0	
Parameter for Material	Symbol	Granite (m1, m2)	Gabbro (m2)
Penny-shaped cracks radius (m)	a_0	60 or ~ 0	60
Volume density of cracks ($\times 10^{-7}$ #/m^3)	N_v	1.68 or 3.36	1.68
Density	ρ	2.7×10^3	3×10^3
S-wave speed (m.s^{-1})	c_s	3.12×10^3	3.25×10^3
P-wave speed (m.s^{-1})	c_p	5.6×10^3	5.84×10^3

experiments for a large range of rocks [*Byerlee*, 1978]. Then, following high strain-rate experiments at range covering earthquake slip rate, we assign a value of 0.1 for the dynamic friction coefficient [*Wibberley et al.*, 2008].

To promote dynamic rupture, we create a nucleation-prone patch in the middle of the fault (see blue line in Figure 14.1), for which τ_0 is defined to be just above the fault strength (~0.03% greater). Following *Kame et al.* [2003], the minimum nucleation size L_c determined by the energy balanced for a slip weakening law is

$$L_c = \frac{16}{3\pi}\frac{\mu G}{\left(\tau^0 - \tau_d\right)^2} = \frac{64}{9\pi^2}\left(\frac{\tau_s - \tau_d}{\tau^0 - \tau_d}\right)^2, \quad (14.48)$$

where

$$\tau_s = f_s\left(-\sigma_{zz}\right) \quad \text{and} \quad \tau_d = f_d\left(-\sigma_{zz}\right). \quad (14.49)$$

Here μ is the shear modulus, G is the fracture energy of the medium, and $R_0 = \left(3\pi/4\right)\left[\mu G/(\tau_d - \tau^0)^2\right]$ is the length of the static sleep weakening zone as defined by *Palmer and Rice* [1973]. For our simulations and choice of parameters we set the size of the nucleation patch to be 1.5 km.

14.3.4. Regularization for Bimaterial Effect

Andrews and Ben-Zion [1997] and *Cochard and Rice* [2000] have shown that the problem of slip on bimaterial fault is ill posed. Yet in our simulations, evolution of off-fault damage during the rupture leads to dynamic changes of elastic moduli, which creates a damage-related material contrast across the fault. Moreover, the effect of off-fault damage on dynamic rupture has been explored for both homogeneous and dissimilar material. To provide a regularization to the ill-posed problem in such scenarios, a characteristic time or slip scale of normal stress response has been proposed [*Cochard and Rice*, 2000; *Ranjith and Rice*, 2001]. Following *Rubin and Ampuero* [2007], we adopt a simplified form of the *Prakash and Clifton* [1993] law, where the fault strength is assumed to be proportional to a modified normal stress σ^*, which evolves toward a residual value over a time scale t^* in response to abrupt change of the actual fault normal stress:

$$\dot{\sigma}^* = \frac{1}{t^*}\left(\sigma - \sigma^*\right). \quad (14.50)$$

Ideally, t^* should be much larger than the time step during the simulation (Δt) yet much smaller than the time to undergo slip weakening, T. Here we use $t^* = 4\Delta x/c_s \simeq 40 \times 10^{-3}$ s.

Another possibility to reduce numerical oscillations is to add an artificial Kelvin-Voigt visco-elastic layer around the fault [e.g., *Brietzke and Ben-Zion*, 2006; *Xu et al.*, 2012, 2014]. However, this may also remove true small scale features and modify the response of the off-fault medium by absorbing energy. Therefore, we did not damp the high-frequency numerical noise with such method to avoid tampering the physical response in our models.

14.3.5. Resolution

To properly solve the problem at hand, we need to define a grid spacing Δx that is small enough to resolve the smallest physical length scale. The spatial discretization Δx (distance between two neighbor nodes) is taken so that there are multiple cells to resolve the process zone Λ for a slip-weakening law, the shortest wavelength λ_{min}, and the nucleation stage.

Following *Day et al.* [2005], if we assume that the process zone Λ is small enough to use a small-scale yielding limit of fracture mechanics [*Rice*, 1968] (stress field around Λ dominated by the singular part of the crack front) and if we assume the crack propagation to be steady, for a slip-weakening law Λ can be expressed as

$$\Lambda = \Lambda_0 \varphi^{-1}\left(v_r\right) \quad (14.51)$$

$$\text{with} \quad \Lambda_0 = \frac{9\pi}{32\left(1-v\right)}\frac{\delta_c \rho c_s^2}{\left(f_d - f_s\right)\sigma_{zz}}, \quad (14.52)$$

where Λ_0 is the static value of the process zone ($v_r = 0$) for a mode II rupture and φ^{-1} is a monotonic function of the rupture speed (see *Day et al.* [2005] for details) for details). Consequently, values for the process zone go from Λ_0 to 0, when v_r reaches the limiting speed, which corresponds to the Rayleigh wave speed c_R for a mode-II rupture in homogeneous solid, and the shear-wave speed for mode III (see *Rubin and Ampuero* [2007] for an estimate of the Λ when there is a material contrast across the fault). Λ_0 is therefore a convenient upper bound for the process zone size, and numerical simulation should resolve with more than one spatial element. In our models, to ensure a good resolution for the dynamic phenomena, the domain is discretized into square 600×170 elements with three Gauss-Lobatto-Legendre nodes (Ngll) nonuniformly distributed per element edge. This provides an element size h of 30 m, and a Δx of ~3 m. The grid spacing Δx is much smaller than the element size h ($\approx$ Ngll^2 times smaller) since in SEM code, each element is subdivided onto a nonregular grid of Ngll $\times$ Ngll nodes. Consequently, the process zone is resolved with ~35 spatial elements, or ~316 nodes. This also satisfies a *Bhat et al.* [2012] criterion that requires $h/a < 1$ to properly account for off-fault damage evolution.

Finally, the time step Δt during the simulations is determined from the Courant-Friedrichs-Lewy (CFL) stability criterion:

$$CFL = c_p \Delta t / \Delta x, \qquad (14.53)$$

where c_p is the P-wave speed. For stability, the CFL is taken to be 0.55 in all simulations.

14.4. RESULTS

An important result of this chapter is that we model not only what is happening on the fault plane but also the constitutive response of the surrounding medium to the dynamic rupture. In the following section we explore the dynamics of earthquake rupture and the associated generation of new damage, how it affects both the hosting medium and the rupture propagation, and what are the damage-related features that can be pertinent to interpret geophysical observations. To investigate the intricate feedbacks between off-fault damage generation and earthquake rupture propagation, we start the study with a simple

case, a 2D right-lateral fault inside a homogeneous medium (Granite), where damage is only occurring on one side. Then we increase complexity by first keeping a homogenous elastic medium but with different initial damage on both sides. The last example presented in this study explores the combined effect of a bimaterial fault (Granite/Gabbro) and a damage evolution law. Reference values for the different parameters are summarized in Table 14.2.

14.4.1. Effect of Damage on Dynamic Rupture for a Single Material

To provide an element of comparison, we first discuss the results for a dynamic rupture in a homogeneous solid (typical Granite, see Table 14.2 for properties) with damage evolution only on the top side of the fault (material 1 in Figure 14.2a). The initial flaw size (a, radius of penny-shaped cracks) was assumed to be 60 m for material 1, which scales with secondary fractures that usually surround main faults extending over several tens of kilometers. The volume density of cracks, N_v, was set to be 1.68×10^{-7}, which gives an initial damage density value, D_0, of 0.1. To prevent
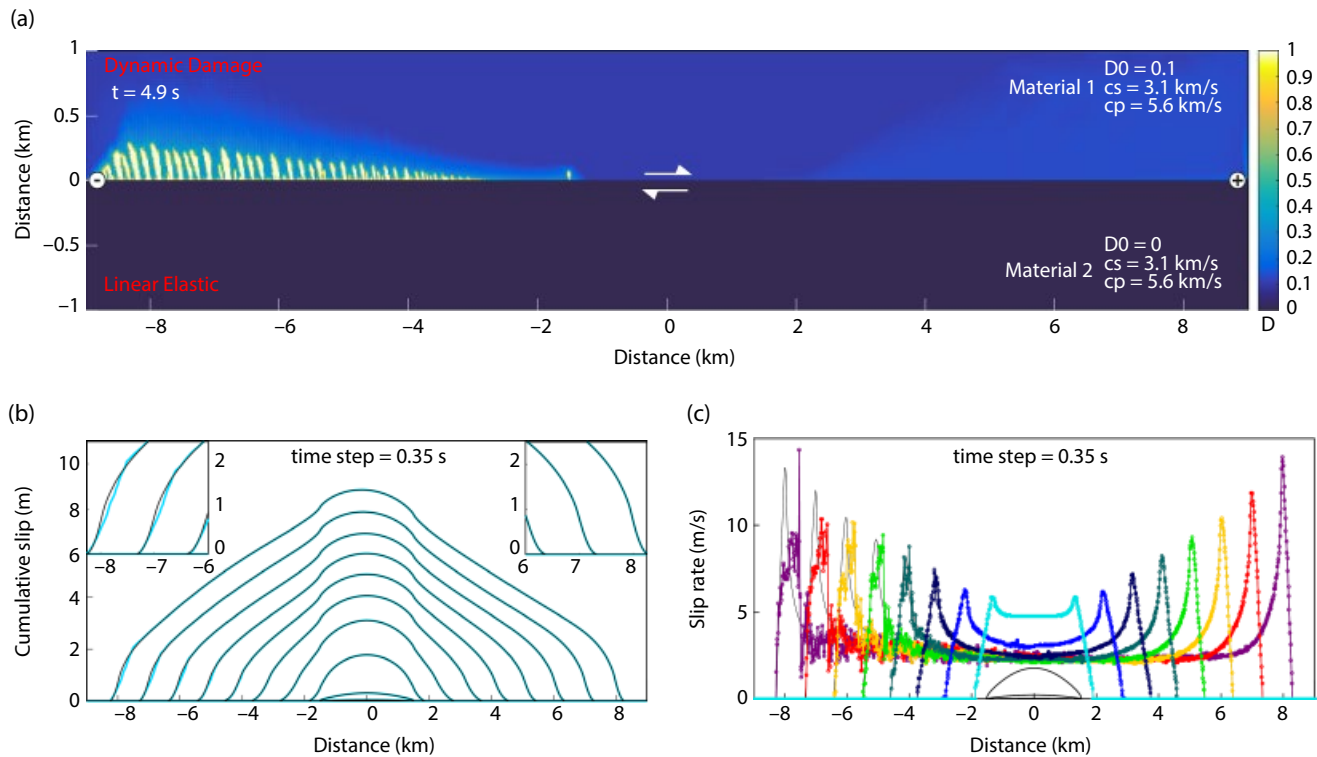

Figure 14.2 Simulation of a dynamic rupture on a right-lateral fault embedded in a homogeneous medium (Granite). We impose a material contrast across the fault by changing the size of the initial microcracks (60 m and 0), which leads to damage evolution on only the top side of the fault. (a) Evolution of the state parameter D (density of microcracks in the medium) at $t = 4.9$ s. Also shown are the "+" and "−" directions as defined in Figure 14.1). Dynamic damage essentially occurs in the tensile quadrant. Cumulative slip (b) and slip rate (c) on the fault are displayed with a time increment of 0.35 s. Colored curves correspond to the dynamic simulation with the damage evolution law; thin black curves depict a simulation with the same parametrization only for a pure elastic medium. *See electronic version for color representation.*

damage from occuring on the bottom side of the fault, we simply assigned a very small initial flaw size for material 2 ($a = 6 \times 10^{-8}$ m). Keeping N_v constant, this returns of value of $D_0 \simeq 0$. As a consequence, the medium on the bottom side of the fault is behaving in a purely elastic manner.

14.4.1.1. Damage Density and Dynamic Changes of Wave Speeds

Figure 14.2a shows a snapshot (at $t = 4.9$ s) of the state parameter D (density of microcracks in the medium),

for a bilateral rupture propagating along the interface between the damaged (above in the graph) and the undamaged material (below). This corresponds to the final stage, at the end of the numerical simulation, chosen to avoid boundary effects. Time evolution of damage with respect to slip rate on the fault is also represented in Figure 14.3. For a right-lateral fault, the rupture tip propagating to the left puts material 1 in tension while the rupture tip on the right induces compression in the medium (T- and C-directions, respectively, in Figure 14.1).
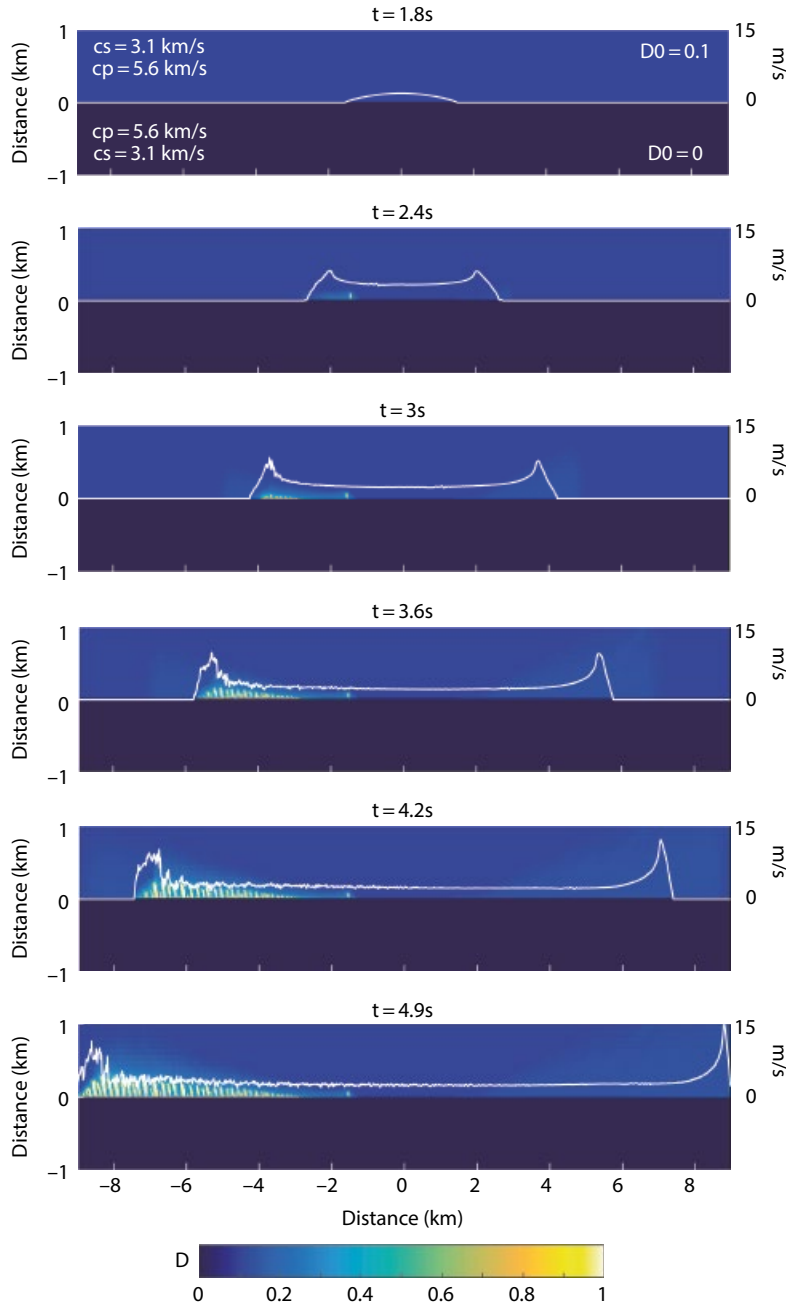

Figure 14.3 Temporal evolution of the damage parameter D for a dynamic rupture on a right-lateral fault embedded in a homogeneous medium (Granite) with damage evolution only on the top side of the fault (see also Figure 14.2). Corresponding slip rate (white) is superimposed on the snapshots. *See electronic version for color representation*.

As illustrated by the parameter D, the response of the damaged elastic solid is different in the compressional and tensional quadrants, with more damage in the tensile lobe. Thus, the rupture traveling on the compressional side activates and/or interacts little with the off-fault damage; whereas on the extensional side, the rupture tip induces a reduction in elastic moduli (Figure 14.4), which differs from a classic bimaterial rupture since the generation of damage induces a dynamic evolution of the elastic properties (or a "dynamic" bimaterial effect). Based on equations (14.37), (14.38), and (14.42), we record a maximum change of 32.7% for S-wave and 28.0% for P-wave. Those results are consistent with geophysical observations of temporal changes in seismic velocity along a natural fault following earthquake ruptures [*Hiramatsu et al.*, 2005; *Li et al.*, 2006; *Brenguier et al.*, 2008; *Cochran et al.*, 2009; *Froment et al.*, 2014]. At the maximum, the width of the newly created damage zone reaches 900 m and corresponds to the location where the higher slip rate has been recorded (Figure 14.2c). However, the extent of the highly damaged zone ($D \geq 0.5$) does not exceed 300 m.

In all our models, we also note the formation of localized damage zones, which is a direct consequence of the constitutive law. This localization of high damage density could be related to the occurrence of branched faults along mature faults. On average, they form a 60° angle with the main fault plane. However, at this stage, caution must prevail and these results should be taken more qualitatively here. Capturing localization accurately in numerical simulations is impossible for constitutive laws that do not have an internal length scale. There are few ways to address this problem, and we are in the process of exploring these remediations. We therefore do not make any conclusions about spacing between branched faults or the width of these localized damage zones.

14.4.1.2. Cumulative Slip, Slip Rate, and Rupture Speed on the Fault

Figures 14.2b and 14.2c display the cumulative slip and slip rate on the fault, respectively, with a time increment of 0.35 s. We compare the model (colored lines) with a right-lateral rupture occurring in a pure elastic medium
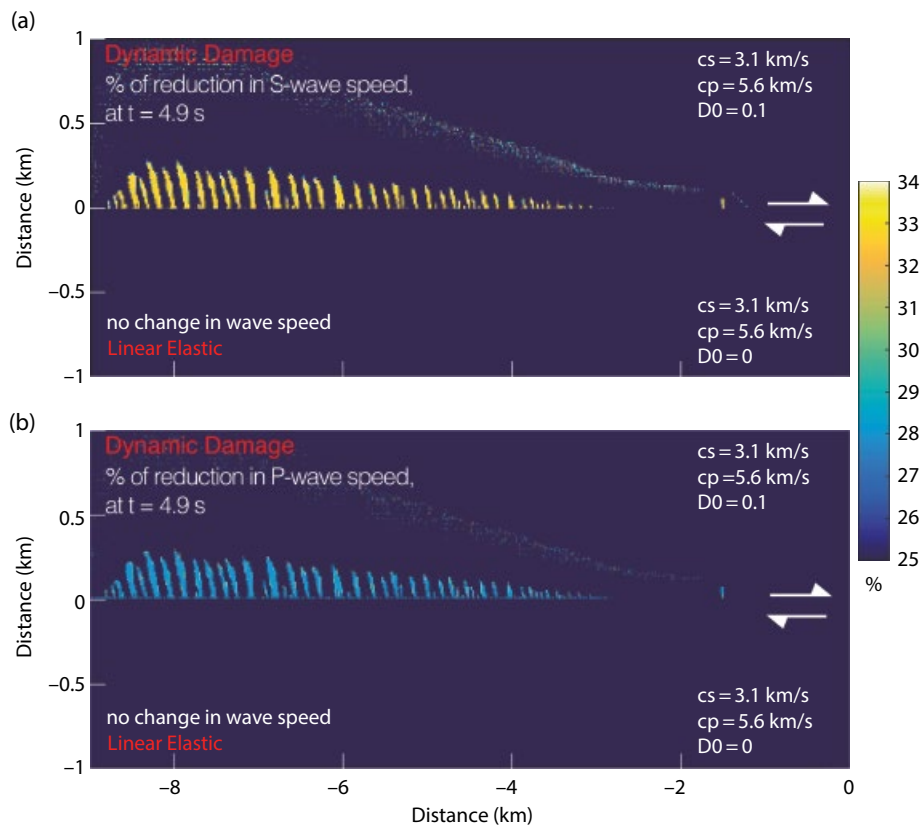

Figure 14.4 Reduction (in %) of S-wave (a) and P-wave (b) speeds in the medium at $t = 4.9$ s, in relation to off-fault damage for a dynamic rupture occuring in a homogeneous medium (Granite) with damage evolution only on the top side of the fault (Figure 14.2). Since evolution of damage essentially occurs on the upper tensile quadrant (Figure 14.2a), we only show that part. Formulas to compute the new c_p and c_s values, based on the regime, are described in equations (14.37), (14.38), and (14.42). For this particular simulation we record a maximum change of 32.7% for S-wave speed and 28.0% for P-wave speed. *See electronic version for color representation.*

(thin black curves). In terms of cumulative slip, we observe little differences with the pure elastic model. In both cases, we record a crack-like rupture and we only observe a small decrease in total slip at the rupture tip, where the widest damage zone was developed (between −8.5 and −6 km, left zoom in Figure 14.2b).

On the other hand, evolution of slip rate along the fault plane strongly differs from a classic elastic model. Figure 14.2c shows that the rupture is bilateral but is asymmetric, with more complexity in the negative direction, which results in high-frequency content in the radiated ground motion (see section 14.4.3). The development of slip rate oscillations is likely related to the development of a low-velocity zone (LVZ), with up to 32.7% drop in wave-speed (Figure 14.4). In fact, we observe that the oscillations occur at some distance behind the rupture front and that they are developed only with the emergence of a damage zone around the fault, in relation to the rupture propagation (Figure 14.3). We also notice that oscillations increase in amplitude as the LVZ becomes larger. As shown by the spacing between symbols on Figure 14.2c, which corresponds to the value at each node, the oscillations of slip rate are well resolved numerically. The development of a material contrast (LVZ) can produce internal wave reflections, which in turn gives rise to an additional feedback mechanism between the evolving off-fault medium and the dynamic rupture [e.g., *Huang et al.*, 2014]. Similar trapped waves were recognized by *Li et al.* [1994] during the 1992 Landers earthquake. From this study, authors estimated a fault zone width of ~180 m, and a strong decrease of fault zone shear velocity (~30%), as observed in our simulations (see in particular results for a bimaterial fault, section 14.4.2.2). However, in regard to the complex pattern of the LVZ, it is hard to evaluate the relative importance of the different parameters on the complicated feedbacks we can observe (e.g., velocity contrast, width, and relative distance between branches, etc).

Finally, in our simulations with damage evolution we observe little modulation of the rupture front, compared to the elastic case. This is because the dynamic rupture, which propagates at subshear velocity on average (~2.7 Km.s^{-1}), interacts with an intact material (Figure 14.3). However, some modulation can be observed, and sometimes the rupture can even reach supershear velocity locally. This is probably related to a process where the radiated waves interact with the LVZ behind the rupture front and further interfere with the rupture front itself.

14.4.2. Evolution of Damage for Dissimilar Materials

For the two following scenarios we chose to increase the complexity by introducing a material contrast across the fault, as usually observed for natural cases. First, we simply keep the same material (Granite) on both sides but assign a different initial damage density (see section 14.4.2.1 and Table 14.2 for details). This could be interpreted as being the cumulative result of dynamic events, propagating dominantly in one direction, which would create a damage contrast across the fault. In the second scenario, we assign different elastic properties on both sides but keep the damage density constant (see section 14.4.2.2 and Table 14.2 for details). For both scenarios, we set the initial microcrack size at 60 m.

14.4.2.1. Variation in Initial Damage Density

For this particular simulation (Figure 14.5a), the elastic properties correspond to those of a typical Granite (Table 14.2), but we change the damage density across the fault: $D_0 = 0.2$ on the top part of the fault (material 1) and $D_0 = 0.1$ for the bottom part (material 2). For an initial microcrack size of 60 m, this leads to a volume density of cracks N_v of 3.36×10^{-7} (#/m^3) and 1.68×10^{-7} (#/m^3), respectively.

Figure 14.5a shows a snapshot of the state parameter D at $t = 4.9$ s, which corresponds to the end of the numerical simulation. Time evolution of damage with respect to slip rate on the fault is also represented in Figure 14.6a. The small initial difference in damage density actively impacts the final result since we observe more dynamic damage generation in the softer material ($D_0 = 0.2$). On the left tensile quadrant, the highly damaged zone ($D \geq 0.5$) extends up to 600 m, whereas in the right tensile lobe, it does not exceed 300 m. We also notice a more "gradual" decay in damage density for material 1. Concurrently, we observe a stronger reduction in elastic properties for the more compliant material (maximum change of 34.4% for S-wave and 28.2% for P-wave) than for the material with less initial damage (maximum change of 32.7% for S-wave and 28.0% for P-wave).

Figures 14.5b and 14.5c display the cumulative slip and slip rate on the fault, respectively, with a time increment of 0.35 s. In accordance with previous observations (section 14.4.1.2), the cumulative slip in the negative direction is slightly smaller than in the positive direction, where less damage is recorded. We also notice slip rate oscillations in both directions. However, they occur earlier in the negative direction, in relation to the development of an LVZ that arises closer to the nucleation prone patch on that part of the fault. Finally, this simulation displays little modulation in the rupture speed, with no significant difference between the two rupture fronts. Again, this is likely related to the fact that the subshear rupture propagates inside an intact material, in both directions.

This simple scenario underlines the importance of incorporating not only the fault history but also the off-fault medium history in dynamic modeling of earthquakes: damage can accumulate over time and influence
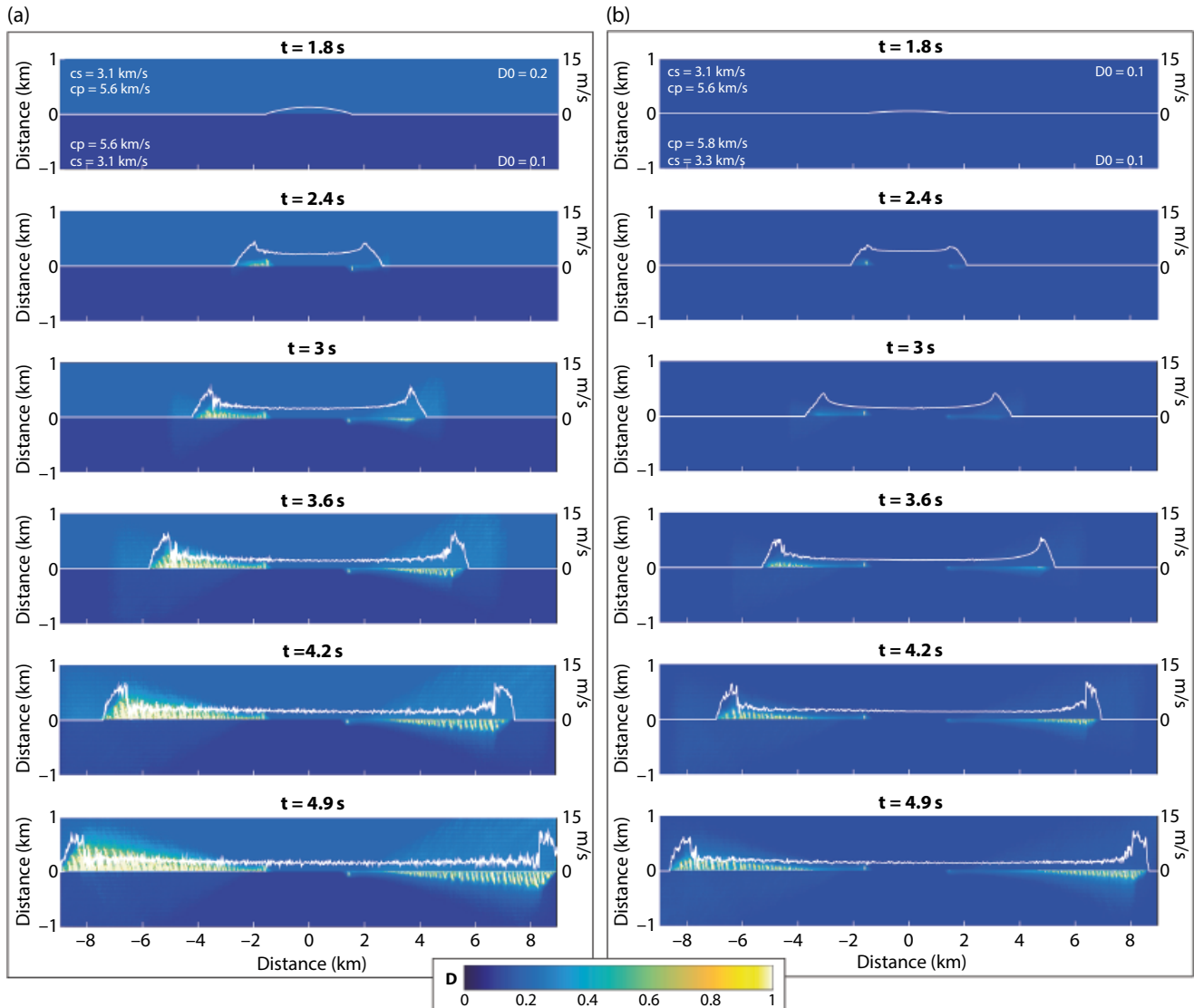
Figure 14.6 Temporal evolution of the damage parameter D for (a) a dynamic rupture on a right-lateral fault embedded in a homogeneous medium (Granite) with a material contrast across the fault by changing the initial damage density (see also Figure 14.5) and (b) a dynamic rupture on a bimaterial fault with the initial damage density of $D_0 = 0.1$ on both sides. Corresponding slip rate (white) is superimposed on the snapshots. *See electronic version for color representation*.

For subshear ruptures, this bimaterial effect instigates a normal stress change behind the rupture tip, with a tensile stress perturbation in the positive direction and a dynamic compression in the opposite direction [e.g., *Rice*, 2002; *Shi and Ben-Zion*, 2006; *Langer et al.*, 2013]. The effect is also sensitive to the degree of material contrast and to the details of static and dynamic friction on the fault plane. In turn, the change in normal stress influences the generation of damage. The compressive perturbation in the negative direction likely explains why the off-fault medium is less damaged when the fault is a bimaterial interface.

Figures 14.7b and 14.7c display the cumulative slip and slip rate on the fault, respectively, with a time increment of 0.35 s. The first subfigure shows a correlation between the size of the LVZ and the importance of cumulative slip reduction, in comparison to the elastic case, like we observed before. In Figure 14.7c, as expected, the material contrast leads to a reduction in slip rate, compared to the homogeneous case (Figure 14.2c). We also notice that the size of the damage zone correlates with the occurrence of slip rate oscillations. They are more important and occurred earlier in the negative direction, in relation to the development of an LVZ that arises closer to the nucleation-prone patch on that part of the fault. As for the previous simulations, there is also very little modulation in the rupture speed, with no significant difference
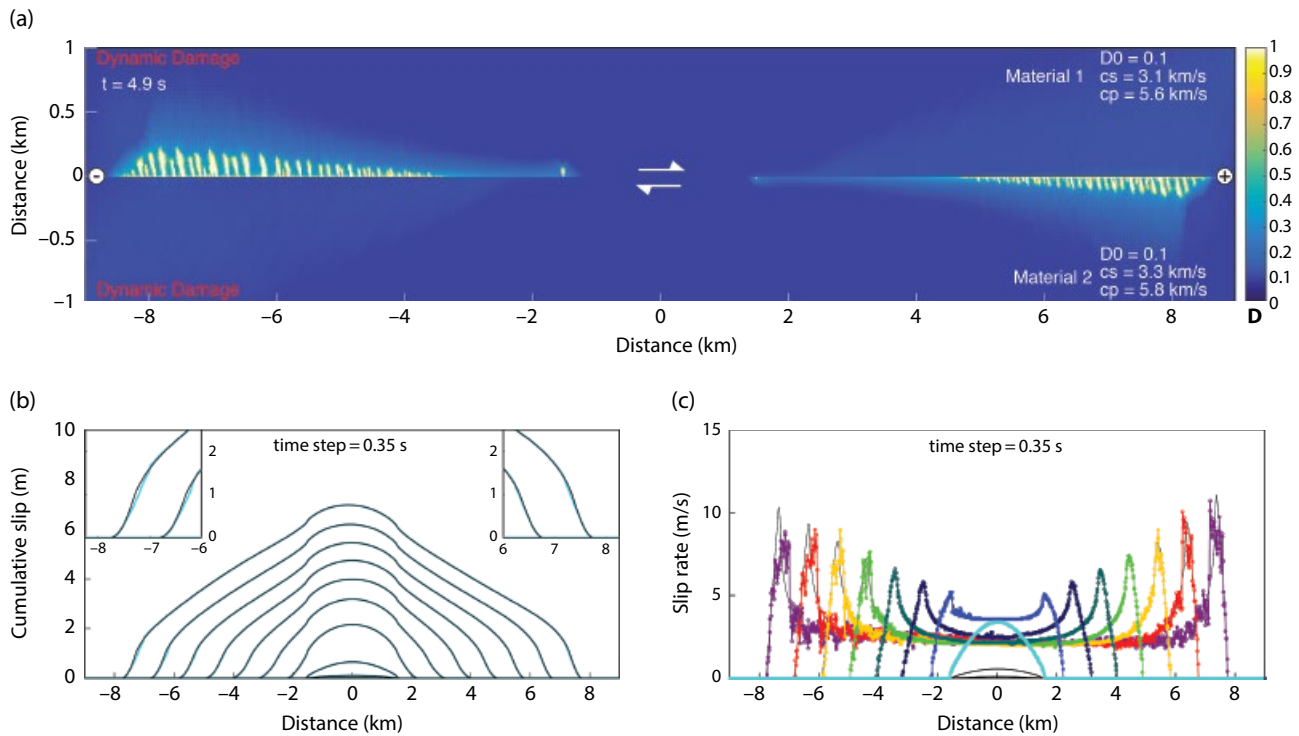
(a)

(b)

(c)

Figure 14.7 Simulation of a dynamic rupture on a bimaterial fault. We impose a material contrast across the fault by changing the elastic properties: Granite on the top side of the fault, and Gabbro on the bottom. In both case, we assign an initial damage density of $D_0 = 0.1$. (a) Evolution of the state parameter D (density of microcracks in the medium) at $t = 4.9$ s. The damage zone is more prominent for the softer material. Also shown are the "+" and "−" directions as defined in Figure 14.1). Cumulative slip (b) and slip rate (c) on the fault are displayed with a time increment of 0.35 s. Colored curves correspond to the dynamic simulation with the damage evolution law; thin black curves depict a simulation for a bimaterial fault embedded in a pure elastic medium. *See electronic version for color representation.*

between the two rupture fronts (rupture propagates inside an intact material, in both directions).

In the different simulations we run, we also explore the case where we have a material and a damage density contrast across the fault (Granite & $D_0 = 0.2$ for material 1 and Gabbro & $D_0 = 0.2$ for material 2). For that particular scenario (not shown here), we basically observe the combined effects described in this section and the section above. The material on the top part of the fault is even more compliant, and we observe a strong difference in damage pattern on both sides of the fault. We also notice that overall less damage is occurring than for the homogenous case (section 14.4.2.1). The broken symmetry in this simulation is the combined result of contrast in elastic properties and the dynamic inelastic asymmetry. The latter depends on whether the tensile or compressive stress concentration lobe is on the side of the fault with a low or high initial damage density. This is coherent with experimental studies that found that fracture damage introduces an additional asymmetry beyond that due to the associated elastic contrast [*Bhat et al.*, 2010; *Biegel et al.*, 2010]. Based on these simulations, one should

expect to see a cumulative effect on the off-fault medium that would produce an asymmetric damage pattern across the fault, which has been observed by *Dor et al.* [2006].

14.4.3. Effects of Damage on Near-Fault Ground Motion

This last section explores the effects of off-fault damage generation on strong ground motion in the near-source region. Figure 14.8 displays synthetic seismograms of fault-parallel and fault-normal velocities for a dynamic rupture on a right-lateral fault embedded in a homogeneous medium (Granite) with different initial damage on both sides of the fault (cf section 4.2.1 and Figure 14.5). For comparison, we also plot the velocities for an elastic medium without damage evolution (colored curves). Seismograms are located on the extensional side and sample the two newly created damaged zones and the medium that has not undergone any reduction in wave speed. As expected for a sub-Rayleigh rupture, the fault-normal component dominates over the fault-parallel component in both cases. Then, if we compare the different
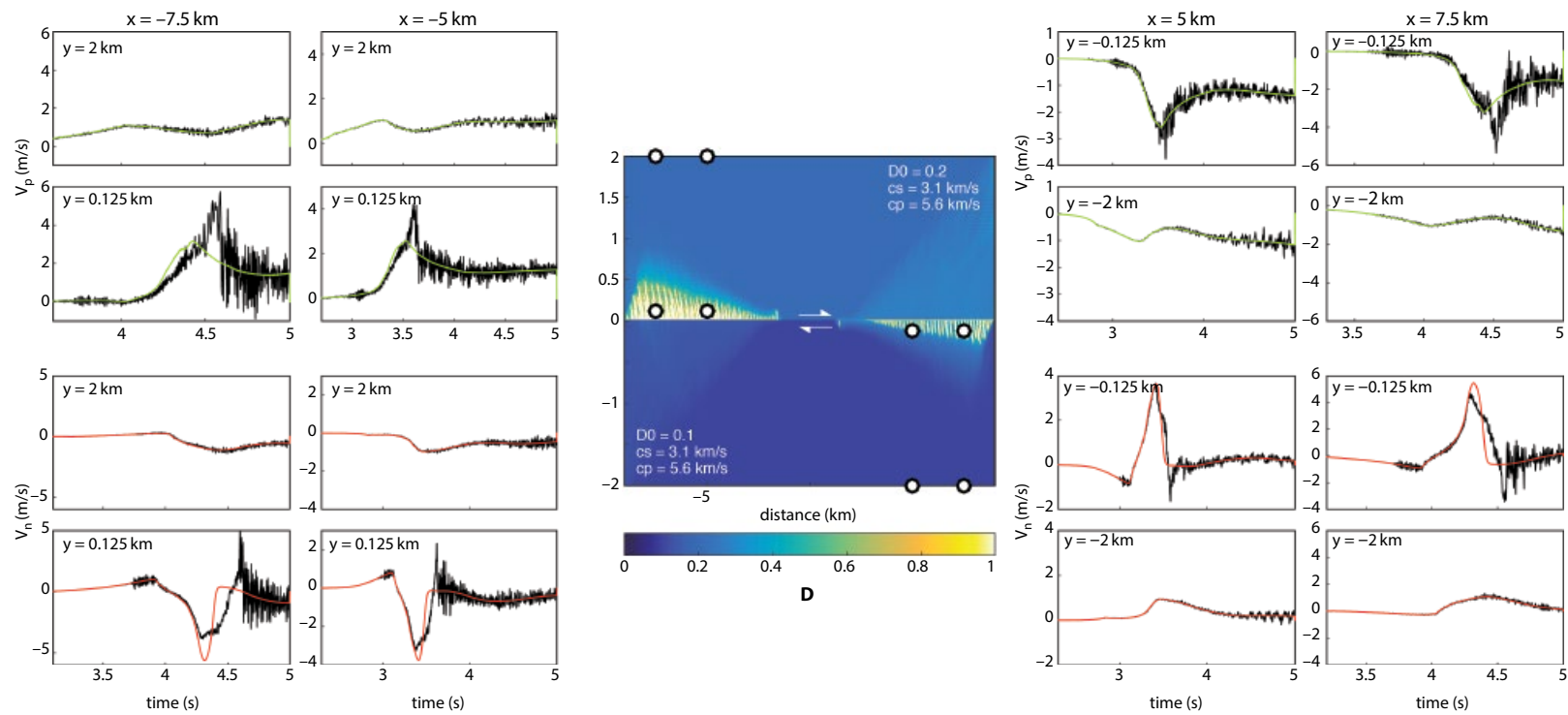
Figure 14.8 Synthetic seismograms of fault-parallel velocity, v_p (eight upper quadrants with green curves), and fault-normal velocity, v_n (eight lower quadrants with red curves). Seismograms are selected so that they sample the damaged and undamaged zones (see the white dots in the middle for location). Black curves correspond to the dynamic simulation with homogeneous elastic properties but different initial damage (section 14.4.2.1 and Figure 14.5). Colored curves correspond to a simulation with the same parametrization but within a pure elastic medium. *See electronic version for color representation*.

seismograms, we observe at first that the four receivers near the fault, inside the LVZs, record long-lived signal oscillations higher in amplitude than the receivers farther away from the fault. We also notice that this phenomenon is even more emphasized for the two receivers located in the softer material, which has undergone a stronger reduction in elastic properties (section 14.4.2.1). Thereafter, if we compare the simulations with a damage evolution's law and those without, we can see that the velocity profiles are superimposed at first, but then there is a strong mismatch in particle velocity behind the rupture front. This is due to the fact that the rupture front propagates at first in an undamaged material. The oscillations and changes in particle velocity we further observe are related to the off-fault reduction in elastic properties due to dynamic damage and the potential reflections of seismic waves in LVZs. As a consequence, the seismograms located farther away from the fault are less likely to be affected by these oscillations than the receivers inside the LVZs, which record more intense ground shaking. Seismic waves are in fact affected by the damage zone at first, but then propagate away in a homogeneous medium.

Figure 14.9 shows the Fourier velocity spectra of the synthetic seismograms displayed in Figure 14.8. For comparison, we also compute the Fourier amplitude spectra (FAS) for a dynamic rupture in an elastic medium without damage evolution (colored curves). If we compare the two models, we can see that incorporating off-fault damage evolution changes the high-frequency content of the seismograms. We observe that between 5 and 100 Hz, Fourier velocity spectra has a higher slope than the elastic case. This contrast is essentially observed for the fault-normal component and to a smaller extent for the fault-parallel component. The difference between the two models is also more pronounced for the receivers that sample the damaged zones than for the ones farther away from the fault. The complexity we observe in slip rate (section 14.4.1.2), together with the change in elastic properties, is responsible for the high-frequency content in the velocity spectra. The additional high-frequency content is most likely due to the localized nature of damage. Since these localized zones are effectively cracks accelerating at a significant fraction of the shear wave speed, they should contribute to the high-frequency content. This is consistent with the near-fault strong motion records of real earthquakes [*Housner*, 1947; *Wald and Heaton*, 1994; *Semmane et al.*, 2005; *Dunham et al.*, 2011] and laboratory experiment observations. Indeed, in his PhD thesis, *Passelègue* [2015] relates the high-frequency radiation recorded during laboratory earthquakes to the amount of damage that was produced. However, in natural cases, damage is not likely the only source

contribution to high-frequency content. *Dunham et al.* [2011] has, for example, demonstrated that fault roughness induces accelerations and decelerations of the dynamic rupture, together with slip heterogeneities, which also result in ground acceleration spectra that are flat at high frequency. With the model we developed, we can explore in future work these combined effects on the radiated ground motion.

14.4.4. Resolution Test

We appraised the robustness of the results discussed in previous sections by comparing simulations with the same parametrization but for different grid resolutions (Figure 14.10). We compare simulations for a dynamic rupture on a right-lateral fault embedded in a homogeneous medium (Granite) with damage evolution only on the top side of the fault for two different mesh sizes: 30 m (as in section 14.4.1) and 15 m. Figure 14.10 displays synthetic seismograms of fault-normal velocity and the corresponding FAS. Although we observe differences in the location and amplitude of the small oscillations (as a result of localization of damage), overall, the velocity profiles are farely well captured (Figure 14.10a–d). Accordingly, the Fourier analyses performed on these seismograms show very similar profiles with the same slope for the two different resolutions (Figure 14.10e–h), supporting further the robustness of the features described in section 14.4. Notably, we observe a similar high-frequency content we relate to dynamic damage generation (section 14.4.3), for the two different resolutions. At this stage, we offer once again a note of caution that our results have to be taken more qualitatively here. As previously underlined in section 14.4.1.1, our constitutive law does not have an internal length scale, which affects the exact localization of damage branches.

14.5. DISCUSSION AND CONCLUSION

In this chapter, we have provided the description of a micromechanical model that accounts for the dynamic evolution of elastic properties in the surrounding medium, related to dynamic off-fault damage. We have numerically investigated the role of spontaneous off-fault damage generation on earthquake rupture processes and underlined damage-related features that can be pertinent to interpret geophysical observations.

The main difference with models allowing for plastic deformation is that the developed constitutive law accounts for dynamic changes of elastic properties in the off-fault medium. These changes of elastic moduli, related to damage generation, have been observed along natural faults during earthquakes and in laboratory experiments
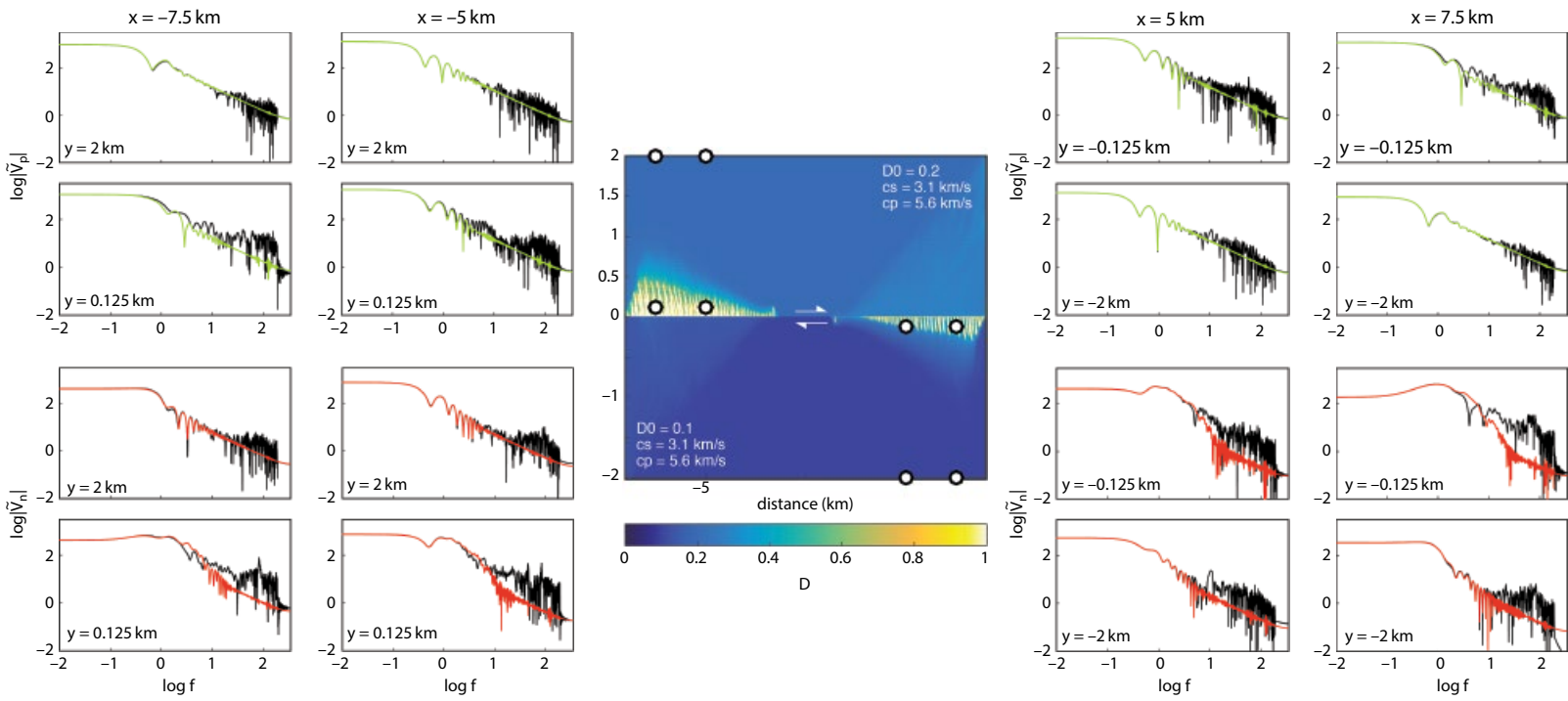
Figure 14.9 Fourier amplitude spectra (FAS) of fault-parallel velocity, v_p (eight upper quadrants with green curves), and fault-normal velocity, v_n (eight lower quadrants with red curves), corresponding to the seismograms in Figure 14.8. Black curves correspond to the dynamic simulation with homogenous elastic properties but different initial damage (section 4.2.1 and Figure 14.5). Colored curves correspond to a simulation with the same parametrization but within a pure elastic medium. Seismograms are selected in order to sample both the damaged and undamaged zones (see the white dots in the middle for location). *See electronic version for color representation*.
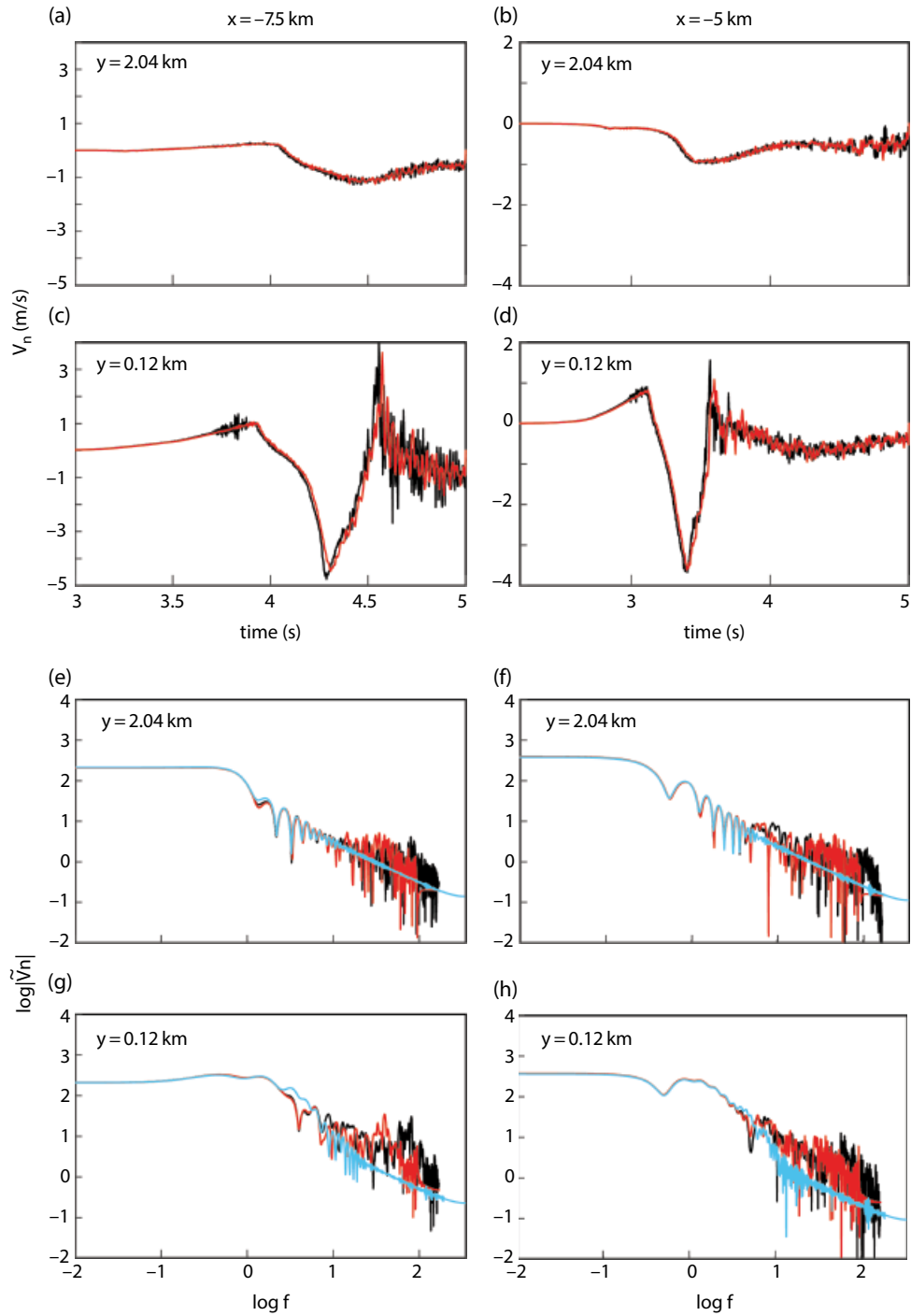
Figure 14.10 Numerical tests on the resolutions of our model with two different mesh sizes. We compare four synthetic seismograms of fault-normal velocity (a–d) and their corresponding FAS (e–h) for a dynamic rupture on a right-lateral fault embedded in a homogeneous medium (Granite) with damage evolution only on the top side of the fault (section 14.4.1 and Figure 14.2). Black and red curves correspond to the dynamic simulations with a 15 m and 30 m mesh size, respectively. For the FAS (e–h), the light blue curves correspond to a simulation with a 30 m mesh size, with the same parametrization but within a pure elastic medium. *See electronic version for color representation.*

REFERENCES

Ampuero, J. P. (2002), Etude physique et numérique de la nucléation des séismes, Ph.D. thesis, Université Paris VII.

Andrews, D. J. (2005), Rupture dynamics with energy loss outside the slip zone, *Journal of Geophysical Research: Solid Earth*, *110*(B1), 307.

Andrews, D. J., and Y. Ben-Zion (1997), Wrinkle-like slip pulse on a fault between different materials, *Journal of Geophysical Research: Solid Earth*, *102*(B1), 553–571.

Andrews, D. J., and R. A. Harris (2005), The wrinkle-like slip pulse is not important in earthquake dynamics, *Geophysical Research Letters*, *32*(23), L23,303.

Ashby, M. F., and C. G. Sammis (1990), The damage mechanics of brittle solids in compression, *Pure and Applied Geophysics*, *133*(3), 489–521.

Audet, P., and R. Burgmann (2014), Possible control of subduction zone slow-earthquake periodicity by silica enrichment, *Nature*, *510*(7505), 389–392.

Ben-Zion, Y., and Z. Q. Shi (2005), Dynamic rupture on a material interface with spontaneous generation of plastic strain in the bulk, *Earth and Planetary Science Letters*, *236*(1-2), 486–496, doi:10.1016/j.epsl.2005.03.025.

Bhat, H., R. Biegel, A. Rosakis, and C. Sammis (2010), The effect of asymmetric damage on dynamic shear rupture propagation II: With mismatch in bulk elasticity, *Tectonophysics*, *493*(3-4), 263–271.

Bhat, H. S., A. J. Rosakis, and C. G. Sammis (2012), A micromechanics based constitutive model for brittle failure at high strain rates, *Journal of Applied Mechanics: Transactions of the ASME*, *79*(3), 031,016.

Bhat, H. S., C. G. Sammis, and A. J. Rosakis (2011), The micromechanics of Westerley granite at large compressive loads, *Pure and Applied Geophysics*, *168*(12), 2181–2198.

Biegel, R., H. Bhat, C. Sammis, and A. Rosakis (2010), The effect of asymmetric damage on dynamic shear rupture propagation I: No mismatch in bulk elasticity, *Tectonophysics*, *493*(3-4), 254–262.

Biegel, R. L., and C. G. Sammis (2004), Relating fault mechanics to fault zone structure, in *Advances in geophysics*, vol. *47*, pp. 65–111, Elsevier.

Brenguier, F., M. Campillo, C. Hadziioannou, N. M. Shapiro, R. M. Nadeau, and E. Larose (2008), Postseismic relaxation along the San Andreas fault at Parkfield from continuous seismological observations, *Science*, *321*(5895), 1478–1481.

Brietzke, G. B., and Y. Ben-Zion (2006), Examining tendencies of in-plane rupture to migrate to material interfaces, *Geophysical Journal International*, *167*(2), 807–819, doi:10.1111/j.1365-246X.2006.03137.x.

Byerlee, J. (1978), Friction of rocks, *Pure and Applied Geophysics*, *116*(4-5), 615–626.

Cappa, F., C. Perrin, I. Manighetti, and E. Delor (2014), Off-fault long-term damage: A condition to account for generic, triangular earthquake slip profiles, *Geochem. Geophys. Geosyst.*, *15*(4), 1476–1493.

Chen, R., K. Xia, F. Dai, F. Lu, and S. Luo (2009), Determination of dynamic fracture parameters using a semi-circular bend technique in split Hopkinson pressure bar testing, *Engineering Fracture Mechanics*, *76*(9), 1268–1276.

Chester, F. M., J. P. Evans, and R. L. Biegel (1993), Internal structure and weakening mechanisms of the San Andreas fault, *Journal of Geophysical Research: Solid Earth*, *98*(B1), 771–786.

Chester, F. M., and J. M. Logan (1986), Implications for mechanical properties of brittle faults from observations of the Punchbowl fault zone, California, *Pure and Applied Geophysics*, *124*(1), 79–106, doi:10.1007/BF00875720.

Childs, C., T. Manzocchi, J. J. Walsh, C. G. Bonson, A. Nicol, and M. P. Schpfer (2009), A geometric model of fault zone and fault rock thickness variations, *Journal of Structural Geology*, *31*(2), 117–127.

Cochard, A., and J. R. Rice (2000), Fault rupture between dissimilar materials: Ill-posedness, regularization, and slip-pulse response, *Journal of Geophysical Research: Solid Earth*, *105*(B11), 25,891–25,907.

Cochran, E. S., Y. G. Li, P. M. Shearer, S. Barbot, Y. Fialko, and J. E. Vidale (2009), Seismic and geodetic evidence for extensive, long-lived fault damage zones, *Geology*, *37*(4), 315–318.

Collettini, C., C. Viti, S. A. F. Smith, and R. E. Holdsworth (2009), Development of interconnected talc networks and weakening of continental low-angle normal faults, *Geology*, *37*(6), 567–570.

Dai, F., R. Chen, M. Iqbal, and K. Xia (2010), Dynamic cracked chevron notched Brazilian disc method for measuring rock fracture parameters, *International Journal of Rock Mechanics and Mining Sciences*, *47*(4), 606–613.

Dai, F., K. Xia, H. Zheng, and Y. Wang (2011), Determination of dynamic rock mode-I fracture parameters using cracked chevron notched semi-circular bend specimen, *Engineering Fracture Mechanics*, *78*(15), 2633–2644.

Dalguer, L. A., K. Irikura, and J. D. Riera (2003), Simulation of tensile crack generation by three-dimensional dynamic shear rupture propagation during an earthquake, *J. Geophys. Res.*, *108*(B3).

Day, S. M., L. A. Dalguer, N. Lapusta, and Y. Liu (2005), Comparison of finite difference and boundary integral solutions to three-dimensional spontaneous rupture, *Journal of Geophysical Research: Solid Earth*, *110*(B12), B12,307, doi:10.1029/2005JB003813.

den Hartog, S. A. M., C. J. Peach, D. A. M. de Winter, C. J. Spiers, and T. Shimamoto (2012), Frictional properties of megathrust fault gouges at low sliding velocities: New data on effects of normal stress and temperature, *Journal of Structural Geology*, *38*, 156–171.

Deshpande, V. S., and A. G. Evans (2008), Inelastic deformation and energy dissipation in ceramics: A mechanism-based constitutive model, *Journal of the Mechanics and Physics of Solids*, *56*(10), 3077–3100.

Dor, O., T. K. Rockwell, and Y. Ben-Zion (2006), Geological observations of damage asymmetry in the structure of the San Jacinto, San Andreas and Punchbowl faults in Southern California: A possible indicator for preferred rupture propagation direction, *Pure and Applied Geophysics*, *163*(2), 301–349, doi:10.1007/s00024-005-0023-9.

Dunham, E. M., D. Belanger, L. Cong, and J. E. Kozdon (2011), Earthquake ruptures with strongly rate-weakening friction and off-fault plasticity, part 2: Nonplanar faults, *Bulletin of the Seismological Society of America*, *101*(5), 2308–2322.

Faulkner, D. R., T. M. Mitchell, D. Healy, and M. J. Heap (2006), Slip on "weak" faults by the rotation of regional stress in the fracture damage zone, *Nature*, *444*(7121), 922–925.

Faulkner, D. R., T. M. Mitchell, E. Jensen, and J. Cembrano (2011), Scaling of fault damage zones with displacement and the implications for fault growth processes, *J. Geophys. Res.*, *116*(B5).

Finzi, Y., E. H. Hearn, Y. Ben-Zion, and V. Lyakhovsky (2009), Structural properties and deformation patterns of evolving strike-slip faults: Numerical simulations incorporating damage rheology, *Pure and Applied Geophysics*, *166*(10), 1537–1573, doi:10.1007/s00024-009-0522-1.

Froment, B., J. J. McGuire, R. D. van der Hilst, P. Gouedard, E. C. Roland, H. Zhang, and J. A. Collins (2014), Imaging along-strike variations in mechanical properties of the Gofar Transform fault, East Pacific Rise, *Journal of Geophysical Research: Solid Earth*, *119*(9), 7175–7194.

Gabriel, A. A., J. P. Ampuero, L. A. Dalguer, and P. M. Mai (2013), Source properties of dynamic rupture pulses with off-fault plasticity, *Journal of Geophysical Research: Solid Earth*, *118*(8), 4117–4126, doi:10.1002/jgrb.50213.

Gao, G., W. Yao, K. Xia, and Z. Li (2015), Investigation of the rate dependence of fracture propagation in rocks using digital image correlation (DIC) method, *Engineering Fracture Mechanics*, *138*, 146–155, doi:10.1016/j.engfracmech.2015.02.021.

Hill, R., and J. R. Rice (1973), Elastic potentials and structure of inelastic constitutive laws, *Siam Journal on Applied Mathematics*, *25*(3), 448–461.

Hiramatsu, Y., H. Honma, A. Saiga, M. Furumoto, and T. Ooida (2005), Seismological evidence on characteristic time of crack healing in the shallow crust, *Geophys. Res. Lett.*, *32*(9).

Hok, S., M. Campillo, F. Cotton, P. Favreau, and I. Ionescu (2010), Off-fault plasticity favors the arrest of dynamic ruptures on strength heterogeneity: Two-dimensional cases, *Geophysical Research Letters*, *37*, L02,306, doi:10.1029/2009GL041888.

Housner, G. W. (1947), Characteristics of strong-motion earthquakes, *Bulletin of the Seismological Society of America*, *37*(1), 19–31.

Huang, Y., J.-P. Ampuero, and D. V. Helmberger (2014), Earthquake ruptures modulated by waves in damaged fault zones, *J. Geophys. Res. Solid Earth*, *119*(4), 3133–3154.

Kame, N., J. R. Rice, and R. Dmowska (2003), Effects of pre-stress state and rupture velocity on dynamic fault branching, *J. Geophys. Res.*, *108*(B5).

Kanamori, H. (2006), Lessons from the 2004 Sumatra-Andaman earthquake, pp. 1927–1945, Royal Society.

Kaneko, Y., and Y. Fialko (2011), Shallow slip deficit due to large strike-slip earthquakes in dynamic rupture simulations with elasto-plastic off-fault response, *Geophysical Journal International*, *186*(3), 1389–1403.

King, D. S. H., and C. Marone (2012), Frictional properties of olivine at high temperature with applications to the strength and dynamics of the oceanic lithosphere, *Journal of Geophysical Research: Solid Earth*, *117*, B12,203, doi:10.1029/2012JB009511.

Klinger, Y., J.-H. Choi, and A. Vallage (2017), Fault branching and long-term earthquake rupture scenario for strike-slip earthquakes, in *Fault Zone Dynamic Processes: Evolution of Fault Properties During Seismic Rupture*, edited by M. Thomas, H. S. Bhat, and T. Mitchell, this volume, AGU/Wiley.

Langer, S., D. Weatherley, L. Olsen-Kettle, and Y. Finzi (2013), Stress heterogeneities in earthquake rupture experiments with material contrasts, *Journal of the Mechanics and Physics of Solids*, *61*(3), 742–761.

Li, Y.-G., K. Aki, D. Adams, A. Hasemi, and W. H. K. Lee (1994), Seismic guided waves trapped in the fault zone of the Landers, California, earthquake of 1992, *J. Geophys. Res.*, *99*(B6), 11,705–11,722.

Li, Y.-G., P. Chen, E. S. Cochran, J. E. Vidale, and T. Burdette (2006), Seismic evidence for rock damage and healing on the San Andreas fault associated with the 2004 m 6.0 Parkfield earthquake, *Bulletin of the Seismological Society of America*, *96*(4B), S349–S363, doi:10.1785/0120050803.

Lyakhovsky, V., and Y. Ben-Zion (2014), A continuum damage–breakage faulting model and solid-granular transitions, *Pure and Applied Geophysics*, *171*(11), 3099–3123, doi:10.1007/s00024-014-0845-4.

Lyakhovsky, V., Y. Ben-Zion, and A. Agnon (1997a), Distributed damage, faulting, and friction, *Journal of Geophysical Research: Solid Earth*, *102*(B12), 27,635–27,649.

Lyakhovsky, V., Z. Reches, R. Weinberger, and T. E. Scott (1997b), Non-linear elastic behaviour of damaged rocks, *Geophysical Journal International*, *130*(1), 157–166.

Ma, S. (2008), A physical model for widespread near-surface and fault zone damage induced by earthquakes, *Geochem. Geophys. Geosyst.*, *9*(11).

Mitchell, T. M., and D. R. Faulkner (2008), Experimental measurements of permeability evolution during triaxial compression of initially intact crystalline rocks and implications for fluid flow in fault zones, *Journal of Geophysical Research: Solid Earth*, *113*(B11), 412.

Mitchell, T. M., and D. R. Faulkner (2009), The nature and origin of off-fault damage surrounding strike-slip fault zones with a wide range of displacements: A field study from the Atacama fault system, Northern Chile, *Journal of Structural Geology*, *31*(8), 802–816.

Morrow, C. A., D. E. Moore, and D. A. Lockner (2001), Permeability reduction in granite under hydrothermal conditions, *J. Geophys. Res.*, *106*(B12), 30,551–30,560.

Ngo, D., Y. Huang, A. Rosakis, W. A. Griffith, and D. Pollard (2012), Off-fault tensile cracks: A link between geological fault observations, lab experiments, and dynamic rupture models, *J. Geophys. Res.*, *117*(B1).

Niemeijer, A., C. Marone, and D. Elsworth (2010), Fabric induced weakness of tectonic faults, *Geophysical Research Letters*, *37*, L03,304.

Palmer, A. C., and J. R. Rice (1973), The growth of slip surfaces in the progressive failure of over-consolidated clay, *Proceedings of the Royal Society of London A: Mathematical, Physical and Engineering Sciences*, *332*(1591), 527–548, doi:10.1098/rspa.1973.0040.

Passelègue, F. (2015), Experimental study of the seismic rupture., Ph.D. thesis, Laboratoire de Géologie de l'École Normale Supérieure, advisors: Ral Madariaga and Alexandre Schubnel.

Prakash, V., and R. Clifton (1993), Time resolved dynamic friction measurements in pressure shear, *Experimental Techniques in the Dynamics of Deformable Solids*, *165*, 33–48.

Ranjith, K., and J. Rice (2001), Slip dynamics at an interface between dissimilar materials, *Journal of the Mechanics and Physics of Solids*, *49*(2), 341–361.

Rice, J. R. (1968), A path independent integral and the approximate analysis of strain concentration by notches and cracks, *Journal of Applied Mechanics*, *35*(2), 379–386, doi:10.1115/1.3601206.

Rice, J. R. (1971), Inelastic constitutive relations for solids: An internal-variable theory and its application to metal plasticity, *Journal of the Mechanics and Physics of Solids*, *19*(6), 433–455, doi:10.1016/0022-5096(71)90010-X.

Rice, J. R. (1975), Continuum mechanics and thermodynamics of plasticity in relation to microscale deformation mechanisms, in *Constitutive equations in plasticity*, edited by A. Argon, chap. 2, MIT Press, Cambridge, Mass.

Rice, J. R. (2002), New perspectives on crack and fault dynamics, *Mechanics for a New Millennium: Proceedings of the 20th International Congress of Theoretical and Applied Mechanics Chicago, Illinois, USA 27 August–2 September 2000*, pp. 1–24, Springer, Netherlands, Dordrecht.

Rice, J. R., C. G. Sammis, and R. Parsons (2005), Off-fault secondary failure induced by a dynamic slip pulse, *Bulletin of the Seismological Society of America*, *95*(1), 109–134, doi:10.1785/0120030166.

Rubin, A. M., and J.-P. Ampuero (2007), Aftershock asymmetry on a bimaterial interface, *J. Geophys. Res.*, *112*(B5).

Savage, H. M., and E. E. Brodsky (2011), Collateral damage: Evolution with displacement of fracture distribution and secondary fault strands in fault damage zones, *J. Geophys. Res.*, *116*, B03405, doi:10.1029/2010JB007665.

Scholz (2002), *The mechanics of earthquakes and faulting*, Cambridge University Press.

Scholz, C. H. (1998), Earthquakes and friction laws, *Nature*, *391*, 37–42.

Semmane, F., F. Cotton, and M. Campillo (2005), The 2000 Tottori earthquake: A shallow earthquake with no surface rupture and slip properties controlled by depth, *J. Geophys. Res.*, *110*(B3).

Shi, Z., and Y. Ben-Zion (2006), Dynamic rupture on a bimaterial interface governed by slip-weakening friction, *Geophysical Journal International*, *165*(2), 469–484.

Shipton, Z., and P. Cowie (2001), Damage zone and slip-surface evolution over μm to km scales in high-porosity Navajo sandstone, Utah, *Journal of Structural Geology*, *23*(12), 1825–1844.

Sibson, R. H. (1977), Fault rocks and fault mechanisms, *Journal of the Geological Society of London*, *133*(3), 191–213, doi:10.1144/gsjgs.133.3.0191.

Suzuki, T. (2012), Understanding of dynamic earthquake slip behavior using damage as a tensor variable: Microcrack distribution, orientation, and mode and secondary faulting, *J. Geophys. Res.*, *117*(B5).

Templeton, E. L., and J. R. Rice (2008), Off-fault plasticity and earthquake rupture dynamics: 1. dry materials or neglect of fluid pressure changes, *J. Geophys. Res.*, *113*(B9).

Thomas, M. Y., J.-P. Avouac, J.-P. Gratier, and J.-C. Lee (2014a), Lithological control on the deformation mechanism and the mode of fault slip on the Longitudinal Valley fault, *Taiwan, Tectonophysics*, *632*, 48–63.

Thomas, M. Y., J.-P. Avouac, J. Champenois, J.-C. Lee, and L.-C. Kuo (2014b), Spatiotemporal evolution of seismic and aseismic slip on the Longitudinal Valley fault, *Taiwan, Journal of Geophysical Research: Solid Earth*, *119*, 5114–5139.

Vallage, A., Y. Klinger, R. Grandin, H. S. Bhat, and M. Pierrot-Deseilligny (2015), Inelastic surface deformation during the 2013 Mw 7.7 *Balochistan, Pakistan, earthquake, Geology*, *43*(12), 1079–1082.

Vermilye, J. M., and C. H. Scholz (1998), The process zone: A microstructural view of fault growth, *Journal of Geophysical Researc: Solid Earth*, *103*(B6), 12,223–12,237.

Wald, D. J., and T. H. Heaton (1994), Spatial and temporal distribution of slip for the 1992 Landers, California, earthquake, *Bulletin of the Seismological Society of America*, *84*(3), 668–691.

Walsh, J. B. (1965a), The effect of cracks in rocks on Poisson's ratio, *J. Geophys. Res.*, *70*(20), 5249–5257.

Walsh, J. B. (1965b), The effect of cracks on the compressibility of rock, *J. Geophys. Res.*, *70*(2), 381–389.

Wang, L., S. Hainzl, M. Sinan Zeren, and Y. Ben-Zion (2010), Postseismic deformation induced by brittle rock damage of aftershocks, *Journal of Geophysical Research*, *115*(B10), 422.

Wang, Q., F. Feng, M. Ni, and X. Gou (2011), Measurement of mode I and mode II rock dynamic fracture toughness with cracked straight through flattened Brazilian disc impacted by split Hopkinson pressure bar, *Engineering Fracture Mechanics*, *78*(12), 2455–2469.

Wibberley, C. A., G. Yielding, and G. Di Toro (2008), Recent advances in the understanding of fault zone internal structure: A review, *Geological Society, London, Special Publications*, *299*(1), 5–33.

Wilson, J. E., J. S. Chester, and F. M. Chester (2003), Microfracture analysis of fault growth and wear processes, Punchbowl fault, San Andreas system, California, *Journal of Structural Geology*, *25*(11), 1855–1873.

Xu, S., Y. Ben-Zion, and J.-P. Ampuero (2012), Properties of inelastic yielding zones generated by in-plane dynamic ruptures II. Detailed parameter-space study, *Geophysical Journal International*, *191*(3), 1343–1360, doi:10.1111/j.1365-246X.2012.05685.x.

Xu, S., Y. Ben-Zion, J.-P. Ampuero, and V. Lyakhovsky (2014), Dynamic ruptures on a frictional interface with off-fault brittle damage: Feedback mechanisms and effects on slip and

near-fault motion, *Pure and Applied Geophysics*, *172*(5), 1243–1267, doi:10.1007/s00024-014-0923-7.

Yamashita, T. (2000), Generation of microcracks by dynamic shear rupture and its effects on rupture growth and elastic wave radiation, *Geophysical Journal International*, *143*(2), 395–406.

Zhang, Q., and J. Zhao (2013), Effect of loading rate on fracture toughness and failure micromechanisms in marble, *Engineering Fracture Mechanics*, *102*, 288–309.

Zhou, X., and A. Aydin (2010), Mechanics of pressure solution seam growth and evolution, *Journal of Geophysical Research*, *115*(B12), 207.